

Lunar-forming collisions with pre-impact rotation

Robin M. Canup*

Southwest Research Institute, Planetary Sciences Directorate, 1050 Walnut St., Suite 300, Boulder, CO 80302, USA

ARTICLE INFO

Article history:

Received 27 July 2007

Revised 29 February 2008

Available online 28 March 2008

Keywords:

Moon

Impact processes

Planetary formation

Satellites, formation

ABSTRACT

Prior models of lunar-forming impacts assume that both the impactor and the target protoearth were not rotating prior to the Moon-forming event. However, planet formation models suggest that such objects would have been rotating rapidly during the late stages of terrestrial accretion. In this paper I explore the effects of pre-impact rotation on impact outcomes through more than 100 hydrodynamical simulations that consider a range of impactor masses, impact angles and impact speeds. Pre-impact rotation, particularly in the target protoearth, can substantially alter collisional outcomes and leads to a more diverse set of final planet–disk systems than seen previously. However, the subset of these impacts that are also lunar-forming candidates—i.e. that produce a sufficiently massive and iron-depleted protolunar disk—have properties similar to those determined for collisions of non-rotating objects [Canup, R.M., Asphaug, E., 2001. *Nature* 412, 708–712; Canup, R.M., 2004a. *Icarus* 168, 433–456]. With or without pre-impact rotation, a lunar-forming impact requires an impact angle near 45 degrees, together with a low impact velocity that is not more than 10% larger than the Earth's escape velocity, and produces a disk containing up to about two lunar masses that is composed predominantly of material originating from the impactor. The most significant differences in the successful cases involving pre-impact spin occur for impacts into a retrograde rotating protoearth, which allow for larger impactors (containing up to 20% of Earth's mass) and provide an improved match with the current Earth–Moon system angular momentum compared to prior results. The most difficult state to reconcile with the Moon is that of a rapidly spinning, low-obliquity protoearth before the giant impact, as these cases produce disks that are not massive enough to yield the Moon.

© 2008 Elsevier Inc. All rights reserved.

1. Background

The leading theory for the Moon's origin is that it formed as a result of the impact of a Mars-sized object with the early Earth (Cameron and Ward, 1976). Key strengths of the giant impact theory include its ability to account for the Earth–Moon system angular momentum (which implies a terrestrial day of only about 5 h when the Moon formed close to the Earth), and the Moon's relatively low iron abundance compared to other inner Solar System objects. In addition, dynamical models of the final stages of Earth's accretion suggest that large impacts were common (e.g., Agnor et al., 1999).

Three-dimensional hydrodynamical simulations (e.g., Benz et al., 1989; Cameron, 2000; Canup and Asphaug, 2001; Canup, 2004a; Wada et al., 2006) are utilized to identify those impacts capable of simultaneously accounting for the masses of the Earth and Moon, the Earth–Moon system angular momentum, and the low lunar iron content. To date, successful cases involve low-velocity collisions (i.e., having an impact speed within 10% of the Earth's es-

cape velocity) by an impactor containing ~ 11 to 14% of the Earth's mass with an impact angle near 45° (Canup and Asphaug, 2001; Canup, 2004a). Gravitational torques, both among the ejected material and between the ejecta and the distorted post-impact shape of the Earth, are the primary mechanism responsible for placing material into bound circumplanetary orbit following such collisions (Canup, 2004a, 2004b).

Despite their successes in accounting for the bulk properties of the Earth–Moon system, several predictions of prior simulations remain somewhat troubling. First, in all cases the protolunar disk mass is derived predominantly from material originating from the impactor rather than from the protoearth. This is contrary to one key perceived strength of the original giant impact hypothesis: that a Moon formed from material originating in the Earth's mantle would offer a natural explanation for the identical oxygen isotope compositions of the Earth and Moon (e.g., Wiechert et al., 2001). To obtain this isotopic commonality, previous results require either an impactor with an identical O-isotope composition to the Earth prior to the Moon-forming collision (which seems unlikely given the dispersion in known O-isotope compositions of other inner Solar System materials, e.g., Clayton, 1993), or that the protolunar disk material isotopically equilibrated with the Earth's post-impact atmosphere, thereby acquiring the terrestrial O-isotope composi-

* Fax: +1 (303) 546 9687.

E-mail address: robin@boulder.swri.edu.

tion through mixing after the giant impact but before the Moon accreted (Pahlevan and Stevenson, 2007). Both alternatives are more restrictive than a Moon derived primarily from the Earth's mantle would be.

A second issue is that the great majority of successful impacts identified to date produce final system angular momenta that are 10 to 20% larger than that of the current Earth–Moon system, L_{EM} (Canup, 2004a, 2004b). The Earth–Moon system angular momentum would have been somewhat greater in the distant past, but probably within a few to 10% of L_{EM} . De-spinning of the Earth due to tides raised on the Earth by the Sun removes about $0.03L_{EM}$ over 4.5 billion years, assuming the current terrestrial tidal dissipation factor, $Q \sim 12$, and Love number, $k_2 \sim 0.25$ (e.g., Canup et al., 2001). If the Moon experienced a high-eccentricity phase due to temporary capture into the evection resonance with the Sun (Kaula and Yoder, 1976; Touma and Wisdom, 1998), an increase in the lunar eccentricity, e , from an initial circular orbit with semi-major axis a would lead to an angular momentum loss $\Delta L_e \sim M_L(1 - (1 - e^2)^{1/2})\sqrt{GM_\oplus a}$, where M_L and M_\oplus are the masses of the Moon and Earth. For $a \sim 4.6$ Earth radii and $e \sim 0.5$ (example values from Touma and Wisdom, 1998), $\Delta L_e \sim 0.03L_{EM}$.

Finally, previous works assume that the protoearth and impactor were not rotating prior to the Moon-forming collision. However, the same accretionary conditions that make a lunar-forming impact probable also imply that terrestrial protoplanets would have been rotating rapidly and with randomly oriented obliquities due to earlier giant impacts (Agnor et al., 1999). Even in the absence of prior large impacts, terrestrial planets can form with rapid prograde rotations and low obliquities in some situations (Ohtsuki and Ida, 1998; Schlichting and Sari, 2007).

In this work I expand on the parameter space considered by prior simulations by considering the effects of pre-impact rotation, together with a broader range in impact velocities and angles, to assess whether other classes of successful, less-restrictive Moon-forming impacts exist.

2. Constraints

Basic properties that must be accounted for by a successful impact include: (i) a total Earth–Moon system angular momentum, $L_{EM} \equiv 3.5 \times 10^{41}$ g-cm²/s, (ii) a Moon whose mass is $M_L = 7.35 \times 10^{25}$ g = $0.012M_\oplus$, and (iii) a bulk lunar mass abundance of elemental iron in the few to 10% range (e.g., Lucey et al., 1995; Jones and Delano, 1989; Jones and Palme, 2000; Canup, 2004a, 2004b).

If the target and impactor are not rotating prior to impact, the angular momentum delivered by an impactor of mass $M_i \equiv \gamma M_T$ is

$$L_{col} = b' M_T^{5/3} f(\gamma) \sqrt{\frac{2G}{(4\pi\rho/3)^{1/3}}} \left(\frac{v_{imp}}{v_{esc}} \right) \approx 1.3 L_{EM} b' \left(\frac{M_T}{M_\oplus} \right)^{5/3} \left(\frac{\gamma}{0.1} \right) \left(\frac{v_{imp}}{v_{esc}} \right), \quad (1)$$

where $b' \equiv \sin(\xi)$ is the scaled impact parameter, ξ is the angle between the surface normal and the impact trajectory (so that a grazing impact has $b' = 1$ and $\xi = 90^\circ$), M_T is the total colliding mass (impactor + target), γ is the impactor-to-total mass ratio, $f(\gamma) \equiv \gamma(1 - \gamma)\sqrt{\gamma^{1/3} + (1 - \gamma)^{1/3}}$, ρ is the density of the colliding objects, (v_{imp}/v_{esc}) is the ratio of the impact velocity to the mutual escape velocity, $v_{esc} \equiv \sqrt{2GM_T/(R_i + R_{tar})}$ where R_i and R_{tar} are the impactor and target radii, and $v_{imp}^2 = v_{esc}^2 + v_\infty^2$, where v_∞ is the relative velocity of the target and impactor at large separation. Terrestrial accretion simulations find that large impacts with $L_{col} \geq L_{EM}$ have $1.0 \leq (v_{imp}/v_{esc}) \leq 1.6$, with an average $(v_{imp}/v_{esc}) \sim 1.2$ (Agnor et al., 1999).

For a target and/or impactor rotating prior to collision, the total angular momentum is $\vec{L}_{imp} = \vec{L}_{col} + \vec{L}_{spin}$, with $\vec{L}_{spin} = \vec{L}_{spin,tar} + \vec{L}_{spin,i}$. For the case of pre-impact spins aligned or anti-aligned with the collision angular momentum, $(\vec{L}_{col} \cdot \vec{L}_{spin})/(L_{col}L_{spin}) = \pm 1$, and

$$L_{imp} = L_{col} + KM_T R_T^2 [\gamma^{5/3} \omega_i + (1 - \gamma)^{5/3} \omega_{tar}], \quad (2)$$

where $R_T^3 \equiv M_T/(4\pi\rho/3)$ is the radius of a single object containing the total colliding mass, ω_{tar} and ω_i are the pre-impact angular rotation rates of the target and the impactor (with $\omega > 0$ {< 0} if the pre-impact spin is in the same {opposite} rotational sense as the impact), and K is the gyration constant for the colliding objects. The requirement that an impact produces a system with the correct angular momentum (i.e., $L_{imp} \sim L_{EM}$) thus brackets a multi-dimensional parameter space in b' , γ , v_{imp} , ω_{tar} and ω_i , within which cases that also give the correct lunar mass and low Fe-abundance must be identified.

The mass and angular momentum of orbiting material needed to produce the Moon can be estimated by a simple conservation argument. Simulations of lunar accretion from an impact-generated disk (Ida et al., 1997; Kokubo et al., 2000) predict an average initial lunar semi-major axis of approximately $1.2a_R$, where $a_R \equiv 2.456R_\oplus(\rho_\oplus/\rho)^{1/3} \approx 2.9R_\oplus(3.3 \text{ g/cm}^3/\rho)^{1/3}$ is the Earth's Roche limit, and $\rho_\oplus = 5.5 \text{ g/cm}^3$ and $R_\oplus = 6378 \text{ km}$ are the Earth's density and radius. Assuming that all of the disk material will eventually be (1) incorporated into a single satellite with $a \approx 1.2a_R$, (2) removed due to collision with the protoearth as the disk viscously spreads, or (3) lost to escape from bound Earth orbit, conservation of mass and angular momentum implies that an initial disk containing mass M_d and angular momentum L_d will produce a satellite of mass M_S , with (Ida et al., 1997)

$$M_S \approx 1.9L_d/\sqrt{GM_\oplus a_R} - 1.1M_d - 1.9M_{esc}, \quad (3)$$

where M_{esc} is the escaping mass. Equation (3) will be a good approximation over a wide range of disk evolution and satellite accretion time scales, provided that the final state is a moon formed near the Roche limit and there is no additional post-impact source of angular momentum or mass to the disk.

Here I use Eq. (3) to estimate the maximum mass satellite that could accrete from an orbiting disk by assuming $M_{esc} = 0$, and define successful impacts to be those that by this estimate produce a satellite with $M_S \geq M_L$, together with a disk containing $< 10\%$ iron by mass and a final system angular momentum $\leq 1.2L_{EM}$.

3. Approach

Smooth particle hydrodynamics, or SPH (e.g., Lucy, 1977; Benz et al., 1989; Canup and Asphaug, 2001; Canup, 2004a, 2005), is used here to model giant impacts. In SPH, matter is represented by spherically symmetric overlapping 'particles' whose individual evolutions are calculated as a function of time. Each particle represents a quantity of mass of a given composition, whose 3-dimensional spatial extent is specified by a density weighting function known as the kernel, and the characteristic spatial width of the particle, known as the smoothing length, h . For each particle, h is varied to maintain overlap with a desired number of other neighbor particles, thus allowing low-density regions to be smoothly (if coarsely) resolved. Because SPH is a Lagrangian method, tracking mixed materials (iron vs silicate) and particle histories (e.g., whether the mass that constitutes the disk originated from the impactor or the target) is straightforward.

3.1. Equation of state

Simulations describe the evolution of each particle's kinematic (position and velocity) and state (internal energy, density) variables

due to the effects of (1) gravity, (2) compressional heating and expansional cooling, and (3) shock dissipation. The M-ANEOS equation of state is used to relate a particle's specific internal energy and local density to its pressure (Thompson and Lauson, 1972; see also Benz et al., 1989; Melosh, 2000, 2008). ANEOS derives thermodynamic quantities from an approximation of each particle's Helmholtz free energy, with temperature and density as independent variables. Mixed phase states (e.g., a two-phase vapor and liquid) are described by treating the different phases as separate components that are in temperature and pressure equilibrium. As in Canup (2004a), I use the M-ANEOS version, revised by Melosh (2000, 2008) to include the formation of silicate vapor composed of diatomic molecules (e.g., SiO or MgO).

For a fixed set of impact conditions, a simulation using M-ANEOS typically produces a somewhat less massive disk with proportionally more iron compared to that obtained using SPH with the simpler Tillotson equation of state (Tillotson, 1962). The first is due to ANEOS being a more physically realistic equation of state, while the second is due to the differences in density between the representative mantle materials. Tillotson simulations typically consider basalt mantles (with a 2.7 g/cm³ reference density, e.g., Canup and Asphaug, 2001) while ANEOS simulations use a more realistic dunite composition (with a 3.3 g/cm³ reference density). A denser mantle material means that a differentiated ANEOS object has a larger core-to-mantle radius ratio than the same mass Tillotson object with the same fraction of iron, which leads to more iron being placed into orbit with ANEOS for a fixed impact parameter. For detailed comparisons of ANEOS vs Tillotson simulations, see Canup (2004a, Section 5.4) as well as Benz et al. (1989).

3.2. Initial conditions and analysis

I consider differentiated impactors and targets that contain 30% iron and 70% silicate (forsterite) by mass, with initial temperatures set as in the “warm start” cases in Canup (2004a), with surface temperatures ~2000 to 2500 K and central temperatures ~3000 to 4500 K for the targets and impactors. The total number of particles, N , varies between 6×10^4 and 1.2×10^5 per simulation, so that initial smoothing lengths within the protoearth and impactor mantles are on the order of 250 to 350 km. The dynamical outcomes of lunar-forming impacts (i.e., disk mass, disk angular momentum, and disk iron) show no systematic changes as resolution is increased from $N = 60,000$ to $N = 250,000$ (see Appendix A and Canup, 2004a, Section 5.1).

Impacts are modeled for ~1 day of simulated time, at which point the protoearth has assumed an approximately oblate spheroidal shape, and orbiting material has been sheared out into a relatively uniform disk. The determination of whether each particle at the end of a simulation is considered to be in the planet, orbiting, or escaping relies upon an iterative procedure (Canup et al., 2001; Canup, 2004a). While disk particles initially have highly eccentric orbits (e.g., Fig. 5 in Canup, 2004a), energy dissipation due to interactions among the disk material will likely damp orbital eccentricities and inclinations on a time scale short compared to the lunar accumulation time (e.g., Kokubo et al., 2000; Thompson and Stevenson, 1988). For each disk particle of mass m , an equivalent circular orbit of radius a_{eq} is computed from the magnitude of the particle's post-impact angular momentum normal to the equatorial plane of the planet, l , with $l = m\sqrt{GM_p a_{\text{eq}}}$, where M_p is the planet's mass. Those particles with a_{eq} greater than the equatorial radius of the planet are considered to be in the disk.

The orbiting mass is itself a dynamic quantity that varies as disk particles undergo angular momentum exchange and some are scattered onto the protoearth. With time, this behavior is increasingly influenced by numerical effects due to the resolution of the

simulation, specifically the spurious viscosity associated with SPH disk particles interacting over a radial distance determined by their smoothing lengths, which grow large in low-density regions. Such effects should be minimal for SPH runs of ~ a day for the resolutions used here (Canup, 2004a). Recently, Wada et al. (2006) have performed two very high-resolution giant impact simulations using an Eulerian hydrocode in combination with a Tillotson-like equation of state (Tillotson, 1962) and uniform compositions for the target and impactor. The high resolution minimizes artificial spreading of the disk and thus allows for longer simulations. Wada et al. find that for an initial disk composed primarily of condensates (true for lunar-forming impacts), the estimated satellite mass from their simulation that used a grid large enough to track the orbiting material (their Fig. 5, case B') is similar to that obtained using SPH. In addition, they show that the predicted satellite mass at 20-h post-impact is comparable to that found at 120-h post-impact. These findings support prior estimates that numerical artifacts with SPH are minimal for run times of ~ a day (Canup, 2004a), and suggest that this simulation length is sufficient to obtain a good estimate of the disk and satellite mass.

4. Results

In this section, I begin by describing general trends in the outcomes of impacts between non-rotating Mars-sized impactors and target protoearths. I then consider a single collision to which pre-impact rotation in the target or the impactor has been added, and use these results to identify which pre-impact spin orientations have the largest effects on impact outcome for a given impactor mass, impact speed and impact angle. Finally I describe several series of simulations involving pre-impact spin in the target that are constrained so that $L_{\text{imp}} \sim L_{\text{EM}}$. Here I consider the impactor size that is optimal in the no-spin case ($\gamma = 0.13$), as well as smaller impactors ($\gamma = 0.05$ and 0.11) for the case of a prograde-rotating target and larger impactors ($\gamma = 0.15, 0.2$ and 0.3) for the case of a retrograde-rotating target. The properties of the successful lunar-forming candidate impacts are then summarized in Table 1, and the implications for the Earth's rotational state before the giant impact discussed.

4.1. Impact outcomes without pre-impact spin

As described by Eq. (1), an oblique collision by an impactor with $M_i \geq 0.1M_{\oplus}$ can supply the Earth–Moon system angular momentum for a total colliding mass, M_T , comparable to the Earth's mass. Fig. 1 shows results of collisions of non-rotating objects involving $M_i/M_T = \gamma = 0.13$ impactors, including simulations from Canup (2004a) and additional simulations with lower b' and higher ($v_{\text{imp}}/v_{\text{esc}}$) values. For a fixed impactor-to-total mass ratio (γ), the yield of orbiting material generally increases with impact parameter, b' (Fig. 1a). As b' increases, a larger fraction of the impactor grazes past the target during the initial collision. Because torques within this material are primarily responsible for placing material into bound orbits that avoid re-impact with the Earth, the resulting disk mass scales roughly as the square of the mass contained in this portion of the impactor (Fig. 1a, dotted line; see Appendix B) for $(v_{\text{imp}}/v_{\text{esc}}) \leq 1.1$ (purple, blue, and green points in Fig. 1) and $0.4 \leq b' \leq 0.8$. Higher-velocity impacts (yellow, orange, and red points) produce higher disk masses for relatively head-on collisions ($0.4 \leq b' \leq 0.6$) than low velocity impacts, while for oblique collisions ($b' \geq 0.7$), impacts with $(v_{\text{imp}}/v_{\text{esc}}) \geq 1.2$ produce little orbiting mass and escape of most—if not all—of the impactor (also Agnor and Asphaug, 2004).¹

¹ At impact parameters and speeds just below those required for the impactor's escape, a large portion of the impactor remains intact on a very high-eccentricity,

Table 1

Successful simulations involving pre-impact spin in the target or impactor aligned with the collisional angular momentum such that $(\vec{L}_{\text{col}} \cdot \vec{L}_{\text{spin}})/(L_{\text{col}}L_{\text{spin}}) = 1$ (“prograde,” light gray rows) or $(\vec{L}_{\text{col}} \cdot \vec{L}_{\text{spin}})/(L_{\text{col}}L_{\text{spin}}) = -1$ (“retrograde,” dark gray rows; see text for details). Listed are the impactor-to-total mass ratio (γ); total angular momentum (including that in the collision and in pre-impact spin) in units of the current Earth–Moon system angular momentum ($L_{\text{imp}}/L_{\text{EM}}$); the angular momentum in the collision ($L_{\text{col}}/L_{\text{EM}}$); pre-impact spin period in hours (T), where an asterisk indicates a pre-impact spin in the impactor and no asterisk indicates a pre-impact spin in the target; impact velocity in units of the mutual escape velocity ($v_{\text{imp}}/v_{\text{esc}}$); scaled impact parameter (b'); orbiting disk mass in lunar masses (M_d/M_L); disk angular momentum L_d scaled by L_{EM} ; the disk vapor mass fraction (M_v/M_d); percentage of the disk mass originating from the impactor; disk mass fraction of iron; angular momentum of final bound planet–disk system L_F scaled to L_{EM} ; and the predicted maximum mass of the resulting satellite (M_S/M_L , per Eq. (3) with $M_{\text{esc}} = 0$)

Run	γ	$L_{\text{imp}}/L_{\text{EM}}$	$L_{\text{col}}/L_{\text{EM}}$	T	$v_{\text{imp}}/v_{\text{esc}}$	b'	M_d/M_L	L_d/L_{EM}	M_v/M_d	% Imp.	M_{Fe}/M_d	L_F/L_{EM}	M_S/M_L
16b	0.13	1.26	1.23	116	1.00	0.70	1.75	0.32	0.20	81	0.04	1.16	1.46
26	0.11	1.10	1.07	101	1.00	0.70	1.13	0.22	0.17	77	0.02	1.03	1.08
53p	0.13	1.30	1.24	56.1	1.05	0.65	1.28	0.25	0.20	65	0.08	1.08	1.21
32	0.11	1.27	1.06	16.8	1.00	0.70	1.22	0.23	0.15	80	0.03	1.20	1.11
119a	0.13	1.26	1.25	15*	1.00	0.73	1.52	0.33	0.13	87	0.02	1.20	1.52
119b	0.13	1.27	1.25	10*	1.00	0.73	1.34	0.30	0.12	88	0.02	1.18	1.34
119c	0.13	1.28	1.25	5*	1.00	0.73	1.52	0.30	0.10	90	0.05	1.11	1.52
78	0.13	1.12	1.18	60.6	1.00	0.65	1.42	0.25	0.20	76	0.04	1.06	1.11
119d	0.13	1.14	1.25	30	1.00	0.73	1.63	0.31	0.21	84	0.06	1.08	1.52
57	0.13	1.10	1.24	23.4	1.00	0.70	1.62	0.31	0.24	82	0.07	1.03	1.45
119e	0.13	1.08	1.25	20	1.00	0.73	1.51	0.28	0.21	82	0.08	0.99	1.33
82	0.13	1.13	1.32	18	1.05	0.70	1.40	0.29	0.16	85	0.07	1.00	1.40
119f	0.13	1.02	1.25	15	1.00	0.73	1.53	0.28	0.22	83	0.06	0.94	1.31
97	0.15	1.11	1.53	10.7	1.00	0.70	1.52	0.31	0.27	82	0.05	1.04	1.52
99b	0.15	1.11	1.48	8.93	1.00	0.73	1.56	0.30	0.33	85	0.10	1.00	1.48
83	0.20	1.18	1.65	6.33	1.00	0.65	1.70	0.31	0.35	69	0.03	1.14	1.44
91	0.20	1.20	1.76	5.38	1.05	0.65	1.69	0.31	0.36	74	0.10	1.11	1.37
92	0.20	1.10	1.75	4.6	1.05	0.65	1.59	0.28	0.36	73	0.10	1.00	1.23
87	0.20	1.18	1.91	4.1	1.00	0.75	2.08	0.40	0.33	62	0.09	1.10	1.96
119j	0.13	1.24	1.25	15*	1.00	0.73	1.43	0.27	0.25	76	0.06	1.17	1.28
119k	0.13	1.23	1.25	10*	1.00	0.73	1.35	0.26	0.27	73	0.07	1.17	1.21
119l	0.13	1.22	1.25	5*	1.00	0.73	1.29	0.25	0.29	63	0.09	1.16	1.17

Considering only those impacts that produce substantial disks, Fig. 1b shows that at each impact parameter there exists a maximum characteristic impact speed above which an overly iron-rich disk results, and this critical impact speed decreases as b' increases. For a fixed value of $(v_{\text{imp}}/v_{\text{esc}})$, increasing b' generally leads to an increase in the fraction of orbiting iron as a larger fraction of the impactor’s core grazes past the target. A notable exception occurs for impacts with $b' \sim 0.7$ to 0.75, as in these cases a large portion of the impactor’s core gravitationally re-contracts after the initial impact and collides directly with the protoearth (e.g. Fig. 2f from Canup, 2004a), resulting in a substantially reduced fraction of orbiting iron. Thus impact speeds $\geq 1.2v_{\text{esc}}$ produce excessively iron-rich disks ($M_{\text{Fe}}/M_d > 0.1$) except in conjunction with small impact parameters, but such cases produce much less massive disks than their more oblique counterparts. Very oblique ($b' > 0.75$), low-velocity impacts produce massive disks, but they contain too much iron to be viable lunar forming candidates.

Without pre-impact spin, disks containing enough mass to yield the Moon are derived predominantly from the impactor’s mantle, and there is a direct correlation between disk mass and the frac-

tion of the disk originating from the impactor (Fig. 1c). Fig. 1d shows the estimated satellite mass from Eq. (3) for the disk produced by each impact as a function of the final bound system angular momentum, L_F . Most cases that produce a lunar-mass satellite also give planet–disk systems that contain too much angular momentum, even given a generous estimate of 10% possible angular momentum loss over the Earth–Moon system’s history due to solar interactions (Fig. 1d, solid and dotted lines). As the impactor mass fraction (γ) is varied, the orbiting mass increases with γ for a given b' and $(v_{\text{imp}}/v_{\text{esc}})$, and similar overall trends to those seen in Fig. 1 result (see Appendix B; also Canup et al., 2001; Canup, 2004a, 2004b).

To date, the preferred lunar-forming candidate impacts have all involved low-velocity collisions ($v \leq 1.1v_{\text{esc}}$) with $b' \sim 0.7$ (or an impact angle $\xi \sim 45^\circ$), because these produce both an enhanced yield of orbiting material and a reduced fraction of orbiting iron (Canup and Asphaug, 2001; Canup, 2004a). To account for the Earth’s mass and L_{EM} then requires an impactor with $0.11 \leq \gamma \leq 0.14$.

4.2. Pre-impact target and impactor spin with fixed impact velocity, angle, and impactor mass

To isolate the effects of pre-impact spin, a successful case from Canup (2004a) (“Earth 119”) is repeated with the addition of pre-

weakly bound orbit that re-impacts the planet after several days or more, and these cases can require very long simulations. For example, the $b' = 0.75$, $v_{\text{imp}} = 1.1v_{\text{esc}}$ case in Fig. 1 was simulated for 61 h in order to resolve the secondary collision of the impactor.

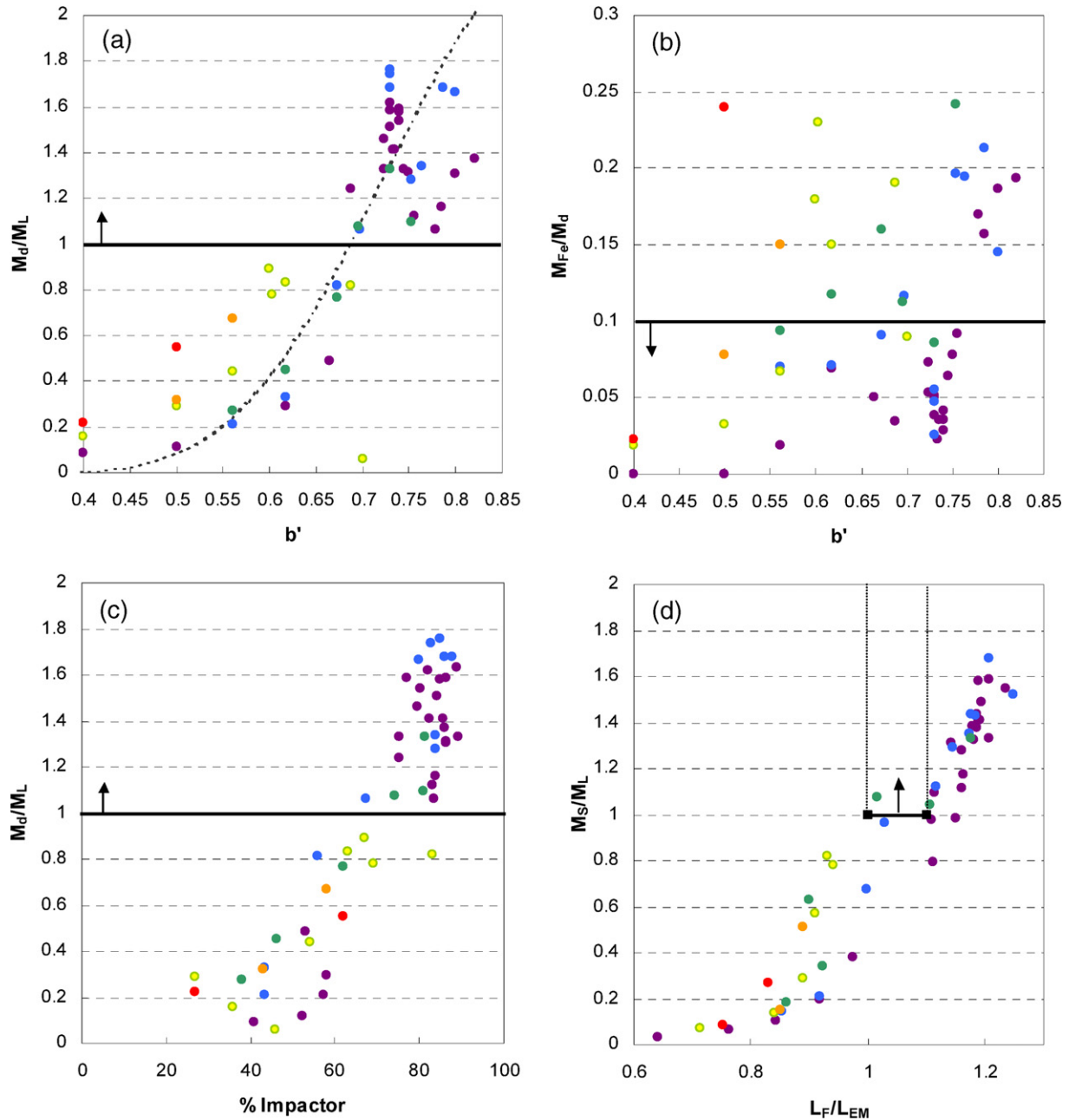


Fig. 1. Results of simulations with $\gamma = 0.13$ and $M_T = 1.019M_\oplus$ for varied scaled impact parameter, b' , and impact speeds, v_{imp} . All objects are non-spinning prior to collision. Color scales with impact velocity, with purple, blue, green, yellow, orange and red points corresponding to $(v_{imp}/v_{esc}) = 1, 1.05, 1.1, 1.2, 1.3,$ and 1.4 , respectively. Bold lines and arrows indicate successful regions of parameter space. (a) Orbiting mass in units of a lunar mass, M_L , as a function of b' . For $(v_{imp}/v_{esc}) \geq 1.2$ and $b' \geq 0.7$, most of the impactor escapes and little if any orbiting mass results. The dotted curve is an analytical prediction from Appendix B, Eq. (B.4). (b) Mass fraction of orbiting iron vs b' . (c) Disk mass in lunar masses vs the percentage of the disk mass originating from the impactor. (d) Predicted maximum satellite mass in lunar masses as a function of the final bound system angular momentum, L_F . Also plotted is the Earth–Moon system (black small squares and black line), with $1 \leq (L_F/L_{EM}) \leq 1.1$ shown to account for loss of angular momentum via solar interactions over the system’s history (see text). An impact that both produces $M_S \geq M_L$ and is consistent with the current Earth–Moon angular momentum would fall between the vertical dotted lines and above the solid black line.

impact rotation in either the target or impactor. The impactor mass ($\gamma = 0.13$ with $M_T = 1.02M_\oplus$), impact speed ($v_{imp} = v_{esc}$), and impact angle ($b' = 0.73$, $\xi = 47^\circ$) are held constant. The resulting impacts have a wide variation in their total angular momentum (with L_{imp} ranging from $0.25L_{EM}$ to $2.25L_{EM}$), so that many would not be appropriate lunar-forming candidates.

I begin with pre-impact spin vectors that are aligned (“prograde”) or anti-aligned (“retrograde”) with the angular momentum vector of the collision. Figs. 2a and 2b show results of cases with $(\vec{L}_{col} \cdot \vec{L}_{spin}) / (L_{col} L_{spin}) = \pm 1$ as a function of $L_{spin} = I\omega$, where ω is the pre-impact angular velocity in the target or impactor and I is

the moment of inertia of either object (calculated assuming a gyration constant equal to that of the Earth, with $K = K_\oplus = 0.335$), with $L_{spin} > 0$ (blue points) and $L_{spin} < 0$ (red points) corresponding to the prograde and retrograde cases, respectively.

For a rotating target, I find relatively minor changes between the cases with pre-impact spin (Figs. 2a and 2b, red and blue squares) and the no-spin case (black square) until the target surface velocity, v_{tar} , reaches a significant fraction of the impact speed (~ 10 km/s). This occurs for cases with $|L_{spin}|/L_{EM} > 0.3$, which have pre-impact target spin periods of 11 h or less and $|v_{tar}| > 1$ km/s. The orbiting mass and angular momentum pro-

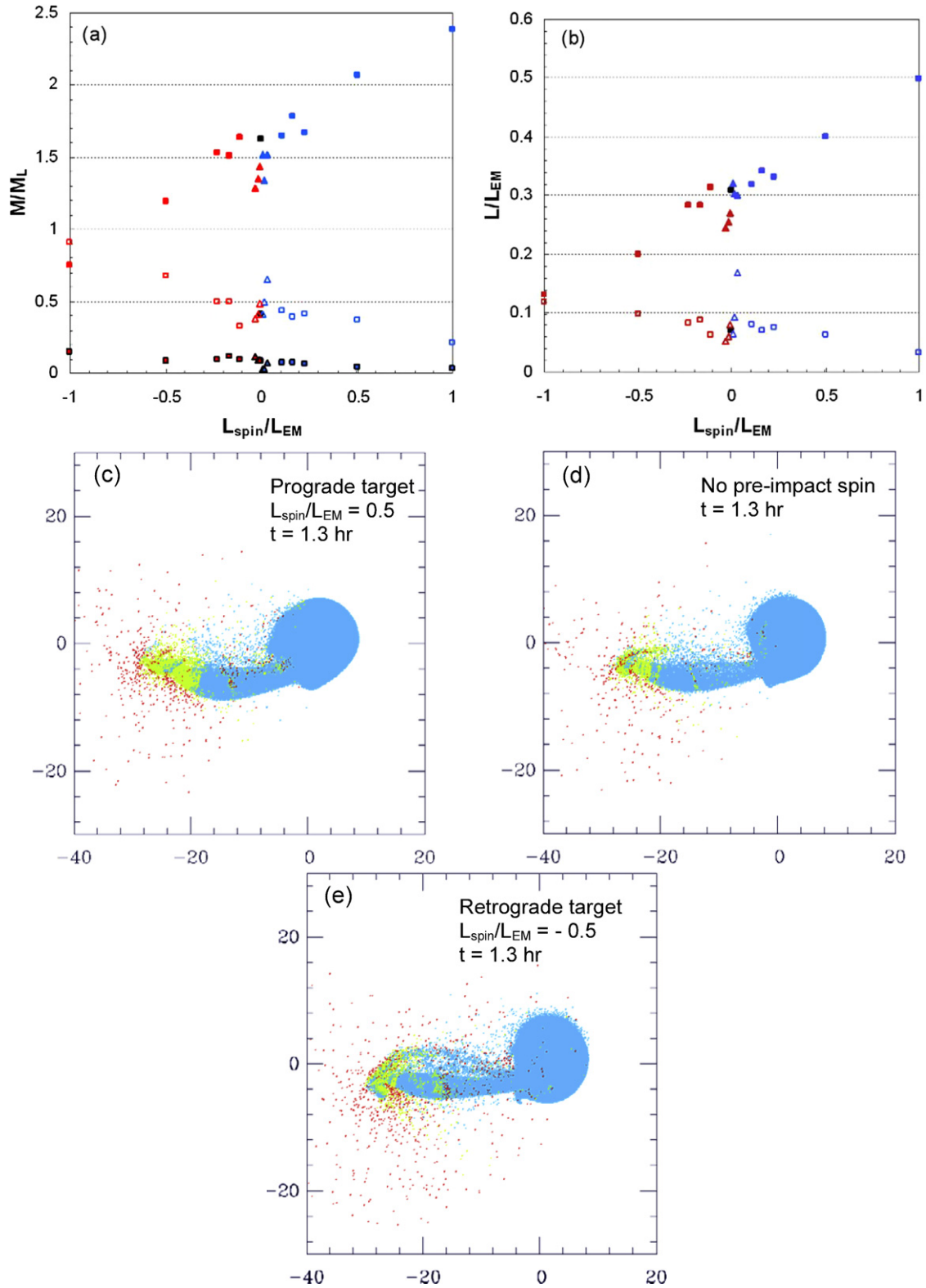


Fig. 2. (a, b) Results of simulations involving the same impactor, target, impact angle, and speed, but with varied pre-impact spin states in the target (squares) or impactor (triangles). Pre-impact targets (impactors) have rotational periods ranging from 3.4 to 30 h (5 to 15 h), and their pre-impact spin vectors are either aligned or anti-aligned with the collision angular momentum vector. A pre-impact spin in the opposite sense of the impact has $L_{\text{spin}} < 0$ (a “retrograde” initial spin, indicated in red), while a pre-impact spin in the same sense of the impact has $L_{\text{spin}} > 0$ (a “prograde” initial spin, shown in blue). Results from the reference simulation in Canup (2004a, Fig. 2) with no pre-impact spin are shown by solid black squares. (a) Orbiting mass (filled symbols), escaping mass (open symbols), and mass of orbiting iron (black outlined filled symbols) in units of a lunar mass, M_L , shown as a function of the pre-impact spin angular momentum, L_{spin} , scaled to the angular momentum of the Earth–Moon system, L_{EM} . (b) Angular momentum in orbiting (filled symbols) and escaping (open symbols) material scaled to L_{EM} shown as a function of $(L_{\text{spin}}/L_{\text{EM}})$. Frames (c)–(e) show the $t = 1.3$ h frame from the three simulations having $(L_{\text{spin}}/L_{\text{EM}}) = 0.5$ (frame c), no pre-impact spin (frame d) and $(L_{\text{spin}}/L_{\text{EM}}) = -0.5$ (frame e). In each case the collision was in the counterclockwise sense. In frames (c)–(e), color represents the fate of the particle at the end of the simulation (blue = accreted by the protoearth, yellow = orbiting in the disk, red = escapes from the protoearth), while distances are shown in units of 10^3 km.

duced by each collision (Figs. 2a and 2b, filled squares) vary approximately linearly with L_{spin} and v_{tar} , with prograde (retrograde) cases yielding more (less) massive disks compared to the no-spin case. The linear dependence on the target's pre-impact angular velocity reflects two processes as described below: (1) momentum exchange between the target and impactor material during the initial impact, and (2) an altered post-impact planet spin rate.

In the hour or so following an oblique, low-velocity collision, the impactor material that has grazed past the target initially forms an elongated structure that is nearly in line with its original trajectory. As this material undergoes Keplerian motion, it is “wound up” into a structure coarsely resembling a trailing spiral arm (e.g., Fig. 2c), and the gravitational torque across this structure allows the outer portions to gain angular momentum and achieve orbit at the expense of the inner portions, which re-collide with the Earth (e.g., Lynden-Bell and Kalnajs, 1972). In addition, the distortion on the surface of the planet from the impact (e.g., Fig. 2c) rotates ahead of the impactor debris, acting akin to a leading tidal bulge to provide a positive torque to the impactor material.

Pre-impact spin in the target affects both processes. Figs. 2c–2e show the same time step from the $L_{\text{spin}}/L_{\text{EM}} = 0.5$ (prograde), the no-spin, and the $L_{\text{spin}}/L_{\text{EM}} = -0.5$ (retrograde) simulations. The outermost portions of the impactor that are farthest from the impact point are affected little by the target's rotation; this material comprises the outer portion of the spiral arm shown in Figs. 2c–2e, which has a similar position in all three runs. However, impactor material originally near the impact site interacts with the prograde rotating target and is imparted a somewhat higher post-impact velocity in the prograde case (Fig. 2c) compared to the no-spin case (Fig. 2d). The direction of its post-impact trajectory is also altered, with its velocity vector rotated in the direction of the target's rotation (counterclockwise for the prograde case). This material is located in the inner-to-middle sections of the trailing arm seen in Fig. 2c, and the change in its velocity due to the target's prograde spin cause it to “lead” the outer arm portions by an increased angle relative to the no-spin case, yielding a somewhat more tightly wound spiral and an increased torque on the outer arm material. A pre-impact prograde target rotation also causes the planet to have a somewhat higher post-impact rotation rate, so that the impact-induced bulge on the planet's surface (seen along the bottom edge of the planet in Fig. 2c) rotates ahead of the impactor material by a larger angle compared to the no-spin case, increasing its torque as well. The net effect of a prograde target spin is then both an increase in the orbiting mass and its characteristic angular momentum. A pre-impact retrograde target spin has the opposite effects, reducing the angle between the outer arm material and both the inner arm material and the impact-induced bulge on the planet's surface (Fig. 2e).

Some fraction of the total colliding mass escapes even for $v_{\text{imp}} = v_{\text{esc}}$. In this case, the escaping material originates predominantly from the most highly-shocked region at the initial impact interface, with this material expanding upon pressure release to velocities exceeding v_{imp} (e.g., Vickery and Melosh, 1987; Canup, 2004a; Figs. 3e–3f). For a $v_{\text{imp}} = v_{\text{esc}}$ impact, the escaping mass is thus sensitive to the relative velocity between the surfaces of contact of the impactor and the target, because this affects the peak shock pressure. A pre-impact prograde spin in the target reduces the relative velocity of the impactor and the target surfaces, leading to somewhat less highly shocked material and therefore less escaping material, while a retrograde spin in the target has the opposite effect of increasing the relative velocity at contact, leading to somewhat more escaping material (Figs. 2a–2b, open squares). For collisions with $v_{\text{imp}} > v_{\text{esc}}$, escaping material also originates from the outer portions of the spiral arm seen in

Figs. 2c–2e, and for such cases the amount of escaping material would tend to increase with increasing prograde target spin, due to effects described in the prior paragraph.

For this $b' \sim 0.7$ collision, the bulk of the impactor's core re-impacts the planet a few hours after the initial impact (Canup, 2004a; Fig. 2f), which removes the majority of the impactor's iron from orbit. A pre-impact retrograde target spin causes this core material to have less angular momentum compared to the no-spin case, so that the secondary collision of the iron core with the planet occurs with a more direct, higher-energy impact, causing somewhat more iron to be ejected outward from this secondary collision into bound planetary orbit (Fig. 2a, red squares outlined in black). Conversely, the prograde cases (blue squares outlined in black) yield a more gentle and grazing collision of the impactor core into the target and a somewhat lower percentage of iron in orbit.

Rotation in the smaller impactor (Figs. 2a–2b, triangles) affects the total angular momentum and therefore collisional outcomes to a lesser degree than pre-impact spin in the target. For the $\gamma = 0.13$ case shown here, an impactor rotational period of 5 h or longer changes the orbiting mass and angular momentum by $\sim 20\%$ or less. The most notable difference is that a prograde-rotating impactor favors the production of a large intact moon, because this spin state tends to counteract the shearing of impactor material due to differential Kepler motion immediately following the initial impact. A similar effect is observed in Pluto–Charon forming collisions (Canup, 2005). While other cases in Figs. 2a and 2b have intact disk clumps containing up to ~ 5 to 10% of a lunar mass, two of the three cases involving a prograde impactor spin produced intact, iron-free moonlets, containing 52 and 74% of a lunar mass and formed nearly entirely from impactor-originating material.

Fig. 3 shows the effects of varying the direction of the target's pre-impact spin axis. With a collision angular momentum defined along the positive z -axis (Fig. 3c), results of cases in which the pre-impact spin axes of the target were aligned or anti-aligned with the x (triangles), y (circles), and z (squares) axes are shown for two target periods of 6.67 and 20 h. A target pre-impact spin that is perpendicular to the collisional angular momentum vector (triangles and circles) has only a modest effect on the final orbiting mass and angular momentum compared to the no-spin case, decreasing these quantities by 10% or less for pre-impact target spin periods > 6 h. For the cases in which \vec{L}_{spin} of the target is orthogonal to $\vec{L}_{\text{col}} = L_{\text{col},z}$, the velocity of the impactor material in the x direction after the initial impact is similar to the no-spin case. The target's spin imparts some motion in the z direction to the material that has direct contact with the target, causing a portion of the trailing arm of impactor material to be rotated out of the x – y plane. Whether this rotation is in the positive or the negative z direction, the net effect is to make the arm structure seen in Figs. 2c–2e somewhat more spatially dispersed so that the torque is decreased. Similarly, rotation of the planet's impact-induced bulge out of the plane of the impact places it somewhat farther away from the impactor material at the end of the arm that is predominantly in the x – y plane, decreasing its associated torque on this material somewhat as well. However these effects are minor compared to those in which the rotation of the planet increases or decreases the velocity of the impactor material in the same direction as the collision itself.

For the rest of the paper, I focus on cases where pre-impact spins in the target are aligned or anti-aligned with the collision angular momentum because other orientations produce both smaller effects and intermediate outcomes.

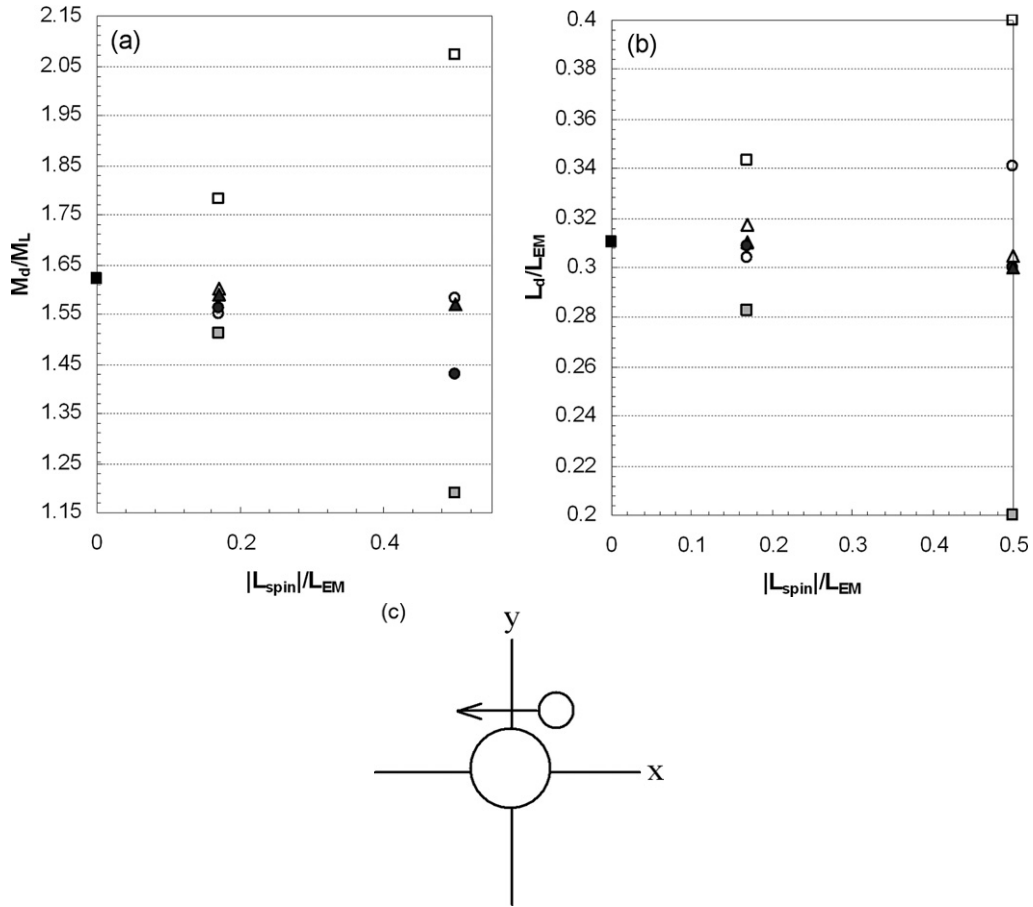


Fig. 3. Results of simulations involving the same impactor, target, impact angle and impact speed as in Fig. 2, but with varied pre-impact spin directions for two initial target spin periods: 6.67 h ($|L_{spin}|/L_{EM} = 0.5$) and 20 h ($|L_{spin}|/L_{EM} = 0.17$). Shown are (a) disk mass in lunar masses and (b) disk angular momentum in units of L_{EM} , both as a function of $|L_{spin}|/L_{EM}$. For all cases, the collisional angular momentum vector is in the direction of the positive z -axis, i.e., $\vec{L}_{col} = L_{col}\hat{z}$ as shown in (c). In (a) and (b) the solid black square is the simulation without pre-impact spin, while the open and gray filled squares correspond to the prograde and retrograde cases from Figs. 2a and 2b that have pre-impact spin angular momenta vectors oriented in the positive and negative \hat{z} directions, respectively. The open and filled circles correspond to pre-impact spin vectors in the positive and negative \hat{y} directions, while the open and filled triangles correspond to pre-impact spin vectors in the positive and negative \hat{x} directions, respectively.

4.3. Pre-impact target rotation with fixed total impact angular momentum

The next simulations explore how collisional outcome depends on the partitioning of a fixed total angular momentum, L_{imp} , between pre-impact spin in the target, the impact parameter, impact velocity, and impactor mass.

4.3.1. Prograde target

For an impact speed comparable to the mutual escape velocity, the loss of angular momentum in escaping material is minor, and so a successful lunar-forming impact requires $L_{imp} \sim L_{EM}$. Compared to a successful case without pre-impact spin, the addition of a prograde pre-impact spin in the target then requires a reduction in the scaled impact parameter, b' , the scaled impact velocity, (v_{imp}/v_{esc}) , and/or the relative mass of the impactor, γ , in order to maintain $L_{imp} \sim L_{EM}$. For $v_{imp} > v_{esc}$, loss of collisional angular momentum in escaping material is more substantial and higher angular momentum collisions can yield a final bound system with $L_F \sim L_{EM}$.

Fig. 4 shows results from 24 simulations that involve the same impactor ($\gamma = 0.13$) as in Figs. 1–3, but with varied pre-impact prograde target rotation, b' , and (v_{imp}/v_{esc}) values; also shown for comparison are 8 simulations without pre-impact spin ($L_{spin}/L_{imp} = 0$). For a fixed L_{imp} (indicated by a given symbol

size) and γ , the disk mass typically decreases as a greater fraction of the impact angular momentum is partitioned into target spin, because this requires that b' and/or (v_{imp}/v_{esc}) are decreased (Fig. 4a). As in the non-spin cases, the disk mass generally increases with impact parameter (Fig. 4b) and the iron mass fraction for a given b' increases as (v_{imp}/v_{esc}) increases (Fig. 4d). All disks that contain a lunar mass or more are composed of more than 60% impactor material (Fig. 4c). Fig. 4e shows that although impacts with high impact speeds and high impact angular momenta (large circles corresponding to $L_{imp} = 1.45L_{EM}$) can yield final systems with $L_F \sim L_{EM}$ after accounting for the loss of angular momentum in escaping material, their disks are either too small in mass or too iron-rich to be Moon-forming candidates.

The successful cases (the four purple and blue points with $M_d > M_L$ in Fig. 4a) that produced both massive and iron-depleted disks with $M_S \geq M_L$ and $M_{Fe}/M_d < 0.1$ had little or no pre-impact rotation (with $L_{spin}/L_{imp} < 0.05$, or a pre-impact target prograde spin period of ~ 55 h or longer), impact angles near 45° (with $0.65 < b' < 0.75$), low impact speeds with $1 \leq v_{imp}/v_{esc} \leq 1.05$, and produced disk masses ranging from 1.1 to $1.75M_L$.

Thus while adding a prograde target spin increases the yield of orbiting material for a given impact configuration (Figs. 2a–2b), when the total impact angular momentum is held constant adding a prograde target spin generally *decreases* the orbiting mass, because it requires a compensating decrease in impact parameter. For

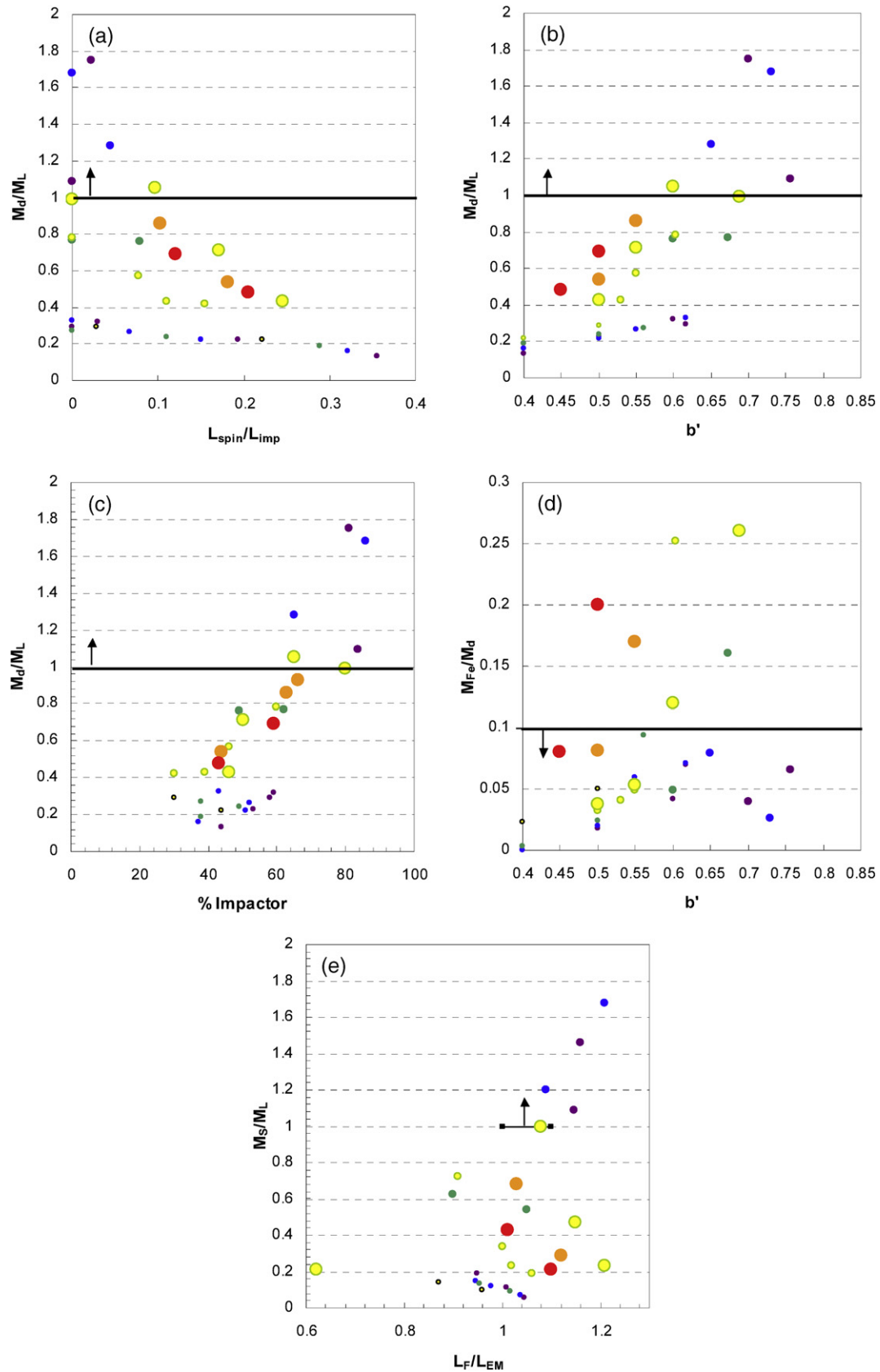


Fig. 4. Results from simulations with $\gamma = 0.13$, $M_T = 1.02M_\oplus$, and a pre-impact prograde spin in the target. Color scales with impact velocity, with purple, blue, green, yellow, orange and red points corresponding to $(v_{imp}/v_{esc}) = 1, 1.05, 1.1, 1.2, 1.3$ and 1.4 , respectively, as in Fig. 1. Bold lines and arrows indicate successful regions of parameter space. Shape size corresponds to total impact angular momentum, with small, medium and large circles corresponding to $L_{imp}/L_{EM} = 1.1, 1.3$ and 1.45 , respectively. (a) Disk mass, M_d , in units of a lunar mass, M_L , as a function of the pre-impact spin angular momentum, L_{spin} , scaled to the impact angular momentum, L_{imp} . (b) Disk mass in lunar masses as a function of b' . (c) (M_d/M_L) vs the percentage of orbiting mass originating from the impactor. (d) Disk iron fraction vs b' . (e) Predicted satellite mass (per Eq. (3)) in lunar masses as a function of the final bound system angular momentum, L_F , scaled to L_{EM} . Shown for comparison is the Earth–Moon system (black small squares and black line).

a given impactor mass, the enhancement in orbiting mass associated with a target's prograde spin and its effects on the spatial distribution of post-impact impactor material is less important than the reduction in orbiting mass caused by having a smaller impact parameter (and therefore a smaller fraction of the impactor's mass grazing past the target).

The angular momentum contribution of a prograde rotating target however allows for low-velocity impacts by smaller impactors to produce $L_{\text{imp}} \sim L_{\text{EM}}$. Fig. 5 shows results of 19 simulations with prograde target spin and smaller impactors with $\gamma = 0.05$ (triangles) and 0.11 (circles). Successful cases with $\gamma = 0.11$ (three of the purple circles having $M_d > M_L$ in Fig. 5a) result for $(v_{\text{imp}}/v_{\text{esc}}) = 1.07 \leq b' \leq 0.75$ and $L_{\text{spin}}/L_{\text{imp}} < 0.20$ (or a pre-impact target prograde spin period of ~ 15 h or longer). Resulting disks with $M_d > M_L$ contain $>75\%$ impactor material by mass (Fig. 5c). The successful smaller impactor cases provide a better match with the Earth–Moon system angular momentum (Fig. 5e) than those in Figs. 1 and 4 with $\gamma = 0.13$, but the $\gamma = 0.11$ disks are less massive, having $1.1 \leq M_d/M_L \leq 1.2$. For $\gamma = 0.05$, disk masses are too small across a wide range of b' and $(v_{\text{imp}}/v_{\text{esc}})$. A rapidly prograde rotating protoearth does not allow for substantially smaller impactors to be viable Moon-forming candidates than those implied by Eq. (1) and simulations without pre-impact spin.

4.3.2. Retrograde target

For a fixed impact angular momentum, a pre-impact retrograde rotation in the target allows for more oblique impacts and/or larger impactors, which are both associated with more massive disks. Fig. 6 contains results of 28 simulations of impacts into retrograde-rotating targets, all with $\gamma = 0.13$. The disk mass often increases as the retrograde target spin is increased, because this allows for increased b' for a fixed total angular momentum (Fig. 6a). Overly iron-rich disks are a common outcome when $(v_{\text{imp}}/v_{\text{esc}}) > 1.1$ and/or $b' \geq 0.75$ (Fig. 6d). The three cases that produce both massive and iron-depleted disks have $|L_{\text{spin}}|/L_{\text{imp}} < 0.15$ (or a pre-impact target retrograde spin period > 18 h), $0.65 \leq b' \leq 0.75$, and $v_{\text{imp}}/v_{\text{esc}} = 1$. Disk masses for these successful cases ranged from 1.1 to $1.6M_L$, and all disks having $M_d/M_L > 1$ are comprised of $>75\%$ impactor material (Fig. 6c). These ranges are similar to the successful non-spin and prograde target spin cases described above. However, the successful retrograde target cases differ in that they produce lower final angular momentum systems with $L_F \sim L_{\text{EM}}$ (Fig. 6e).

Fig. 7 shows results of 20 simulations involving larger impactors with $\gamma = 0.15$ (triangles), $\gamma = 0.20$ (circles), and $\gamma = 0.30$ (squares). Six produced successful outcomes, with these cases having $|L_{\text{spin}}|/L_{\text{imp}} < 0.60$ (or a pre-impact target retrograde spin period of ~ 4.1 h or longer), $0.65 \leq b' \leq 0.75$ and $1 \leq v_{\text{imp}}/v_{\text{esc}} \leq 1.05$. As seen here and in the simulations in Figs. 1, 4 and 6, impacts with $v_{\text{imp}}/v_{\text{esc}} = 1.2$ (yellow symbols) and $b' \approx 0.6$ can give nearly successful results, but consistently produce disks that contain insufficient mass and/or too much iron to yield the Moon. The disk masses for the six successful cases ranged from 1.5 to $2.1M_L$, and are composed of $>60\%$ impactor material. In an extreme case of $\gamma = 0.3$ and a target with a pre-impact spin period of just 1.98 h, a disk with $M_d/M_L > 1$ and composed of only 45% impactor material resulted (Fig. 7c). This was the only disk having $M_d/M_L > 1$ produced by any of the simulations that contained a majority of target-originating material, but it also produced an overly iron-rich disk with $M_{\text{Fe}}/M_d = 0.19$.

Thus larger impactors ($\gamma \sim 0.15$ to 0.2) are plausible if the protoearth had a substantial retrograde spin prior to the Moon-forming impact. As with the successful simulations in Fig. 6, those in Fig. 7 produce a closer agreement between L_F and L_{EM} than the no-spin cases (Fig. 1). Oblique collisions by still larger impactors with $\gamma = 0.3$ (Fig. 7, magenta points) require very rapid retrograde

pre-impact target rotation with periods less than 3 h to produce final systems having $L_{\text{imp}} \sim L_{\text{EM}}$, and these produced overly iron-rich disks.

Note that because most pre-impact spin orientations would have a reduced influence on impact outcome relative to the extreme orientations simulated in Figs. 4 through 7, and given that the potential parameter space is not evenly sampled, the number of successful vs unsuccessful cases in Figs. 4–7 does not indicate overall probability of a successful impact.

4.4. Properties of successful lunar-forming candidate impacts

Table 1 lists simulations involving pre-impact rotation with $(\vec{L}_{\text{col}} \cdot \vec{L}_{\text{spin}})/(L_{\text{col}}L_{\text{spin}}) = \pm 1$ that produced iron-depleted disks, predicted maximum satellites masses $\geq M_L$, and final bound systems with $L_F \leq 1.2L_{\text{EM}}$. Most of the properties of these impacts are similar to those of the successful cases without pre-impact spin (Table 1 in Canup, 2004a). The successful cases with spin display the same range of impact velocities ($v_{\text{imp}}/v_{\text{esc}} < 1.1$) and a very similar range in impact parameter ($0.65 \leq b' \leq 0.75$ vs $0.67 \leq b' \leq 0.76$ for the no-spin cases). The mass fraction of vapor in the disk is somewhat higher on average in the retrograde spin cases—expected because the relative velocity and thus impact energy is enhanced by the sense of the target's spin and because the impactor can be larger—but the overall range of values for this fraction (13 to 36%) for the simulations in Table 1 is similar to that of the no-spin cases (10 to 30%; Canup, 2004a). The percentage of the disk mass that originates from the impactor (62 to 90%) displays a slightly broader range than seen in the no-spin cases (73 to 89%).

The most significant differences occur for cases involving a pre-impact retrograde rotation in the target, which allows for an increase in the range of plausible impactor masses to include those containing up to 20% of the Earth's mass, and produces final systems that on average show an improved agreement with the Earth–Moon system angular momentum. Fig. 8 shows an example of such a case (Run 87), which differs the most morphologically from the simulations depicted in Canup (2004a). This is a relatively extreme case of the collision of a $0.2M_{\oplus}$ impactor with a rapidly retrograde spinning target, whose pre-impact spin period is just 4.1 h with a spin axis anti-aligned with the collisional angular momentum. After the initial impact, the impactor gravitationally re-coalesces into an intact form (Fig. 8d) that then undergoes a secondary collision with the protoearth. The final disk contains 2.1 lunar masses and the planet–disk system has a final angular momentum of $1.1L_{\text{EM}}$. The majority of the disk mass (62%) originates from the impactor (Fig. 8g), and most of the material in both the target and impactor is heated by at least 3000 K relative to its initial temperatures (Fig. 8h).

Fig. 9 shows the simulation involving a pre-impact prograde rotation in the target that produced the largest disk mass of any of the prograde cases (Run 32). In this case, a $\gamma = 0.13$ impactor collides with a target having an initial 56-h day with an impact speed just exceeding the mutual escape velocity. The resulting disk contains 1.28 lunar masses, with a final system angular momentum of $1.08L_{\text{EM}}$. Compared to the larger impactor case shown in Fig. 8, the degree of heating of the target and impactor during the impact here is substantially reduced (Fig. 9h).

4.5. Implications for the pre-impact rotation state of the protoearth

Models of the evolution of the Earth–Moon–Sun system imply a low initial terrestrial obliquity, with $\theta_{\oplus} \sim 7^\circ$ to 15° (Goldreich, 1966; Touma and Wisdom, 1994), which in the context of the giant impact model would reflect the orientation of the system angular

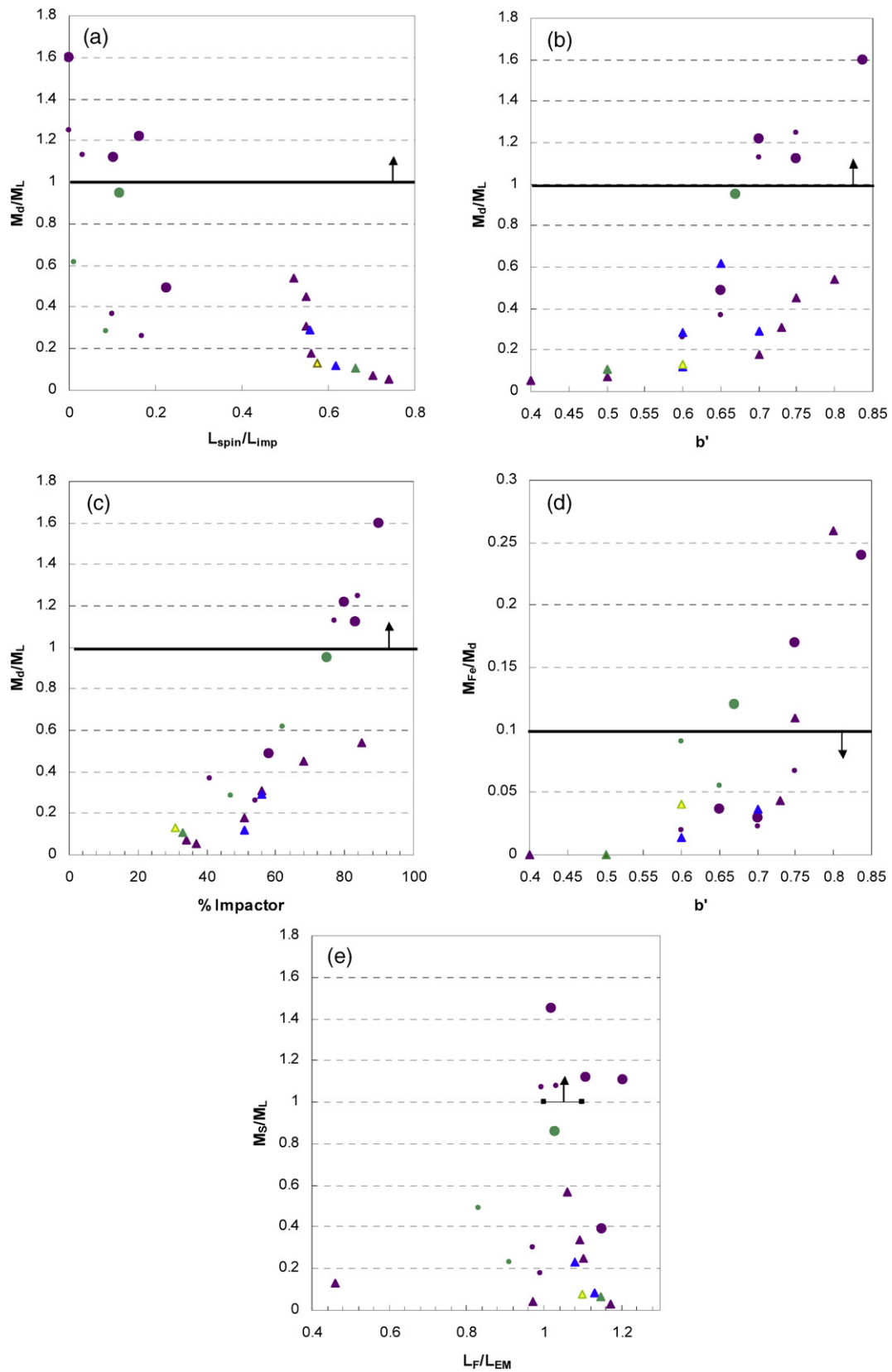


Fig. 5. Results of simulations involving pre-impact prograde target spin in combination with smaller impactors ($\gamma = 0.11$, circles, and $\gamma = 0.05$, triangles). Color scales with (v_{imp}/v_{esc}) as in Figs. 1 and 4, and symbol size varies with impact angular momentum, with small and medium circles corresponding to $L_{imp}/L_{EM} = 1.1$ and 1.3, and medium triangles to $L_{imp}/L_{EM} = 1.2$. Frames (a) through (e) show the same quantities as in Fig. 4.

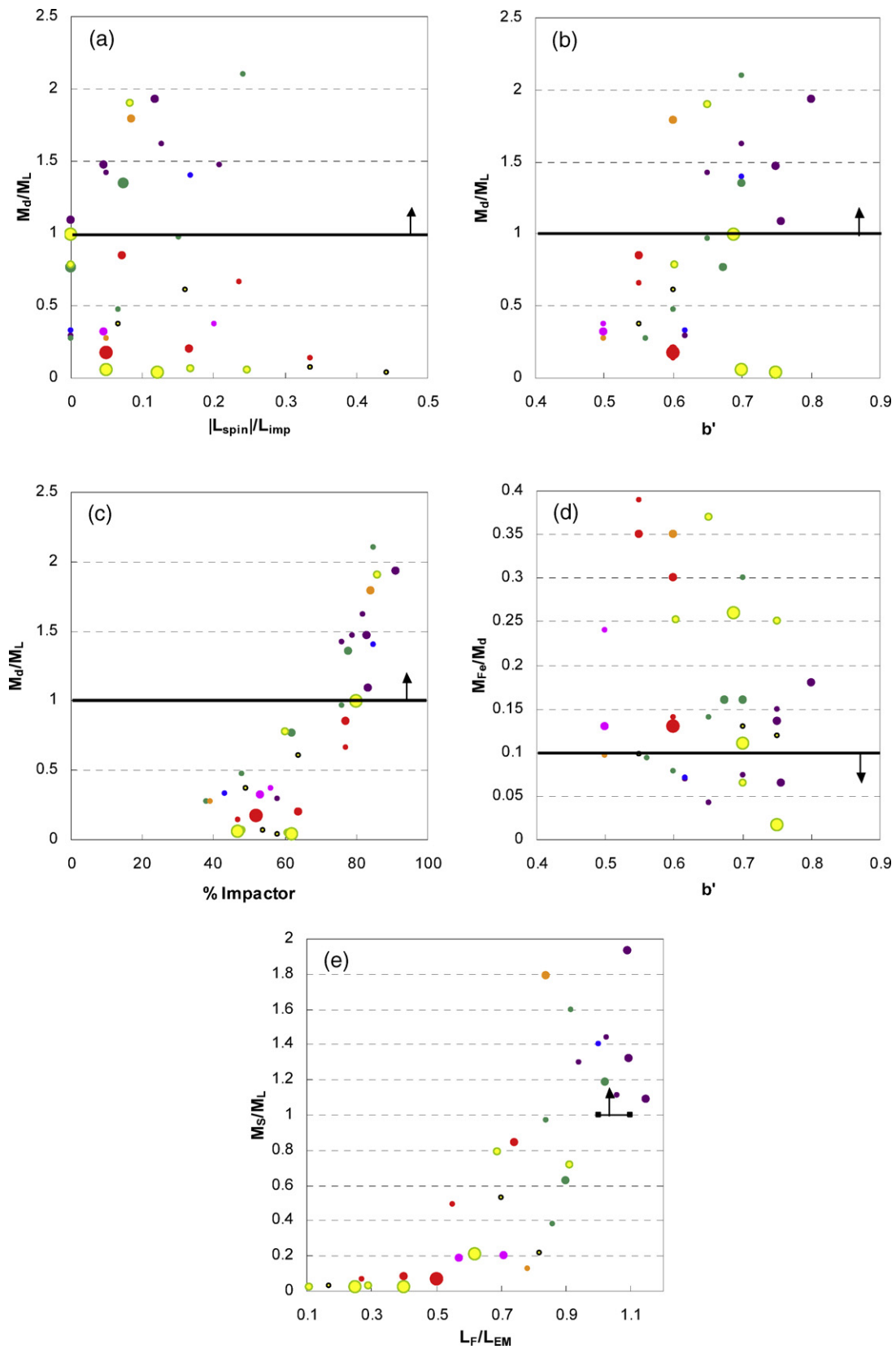


Fig. 6. Results of simulations involving pre-impact retrograde target spins with $\gamma = 0.13$. Color scales with velocity as in Figs. 1, 4 and 5, with the addition of $(v_{imp}/v_{esc}) = 1.5$ points here (pink). Symbol size scales with impact angular momentum, with small, medium and large circles corresponding to $L_{imp}/L_{EM} = 1.1, 1.3$ and 1.45 , respectively. Frames (a) through (e) show the same quantities as in Figs. 4 and 5.

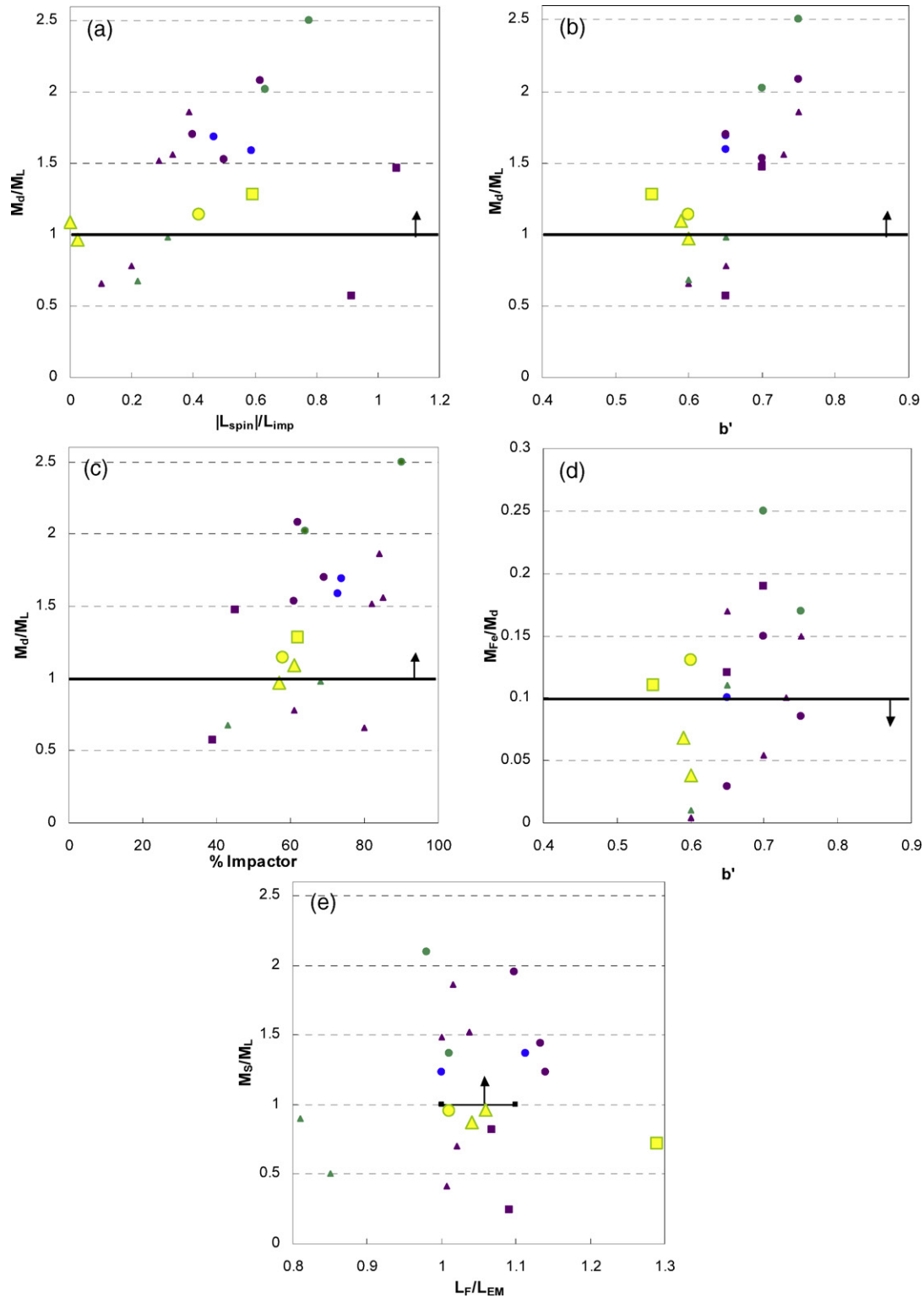


Fig. 7. Results of simulations involving pre-impact retrograde target spin in combination with larger impactors with $\gamma = 0.15$ (triangles), $\gamma = 0.2$ (circles) and $\gamma = 0.3$ (squares). Color scales with impact velocity as in Figs. 1 and 4–6. Small triangles have $L_{\text{imp}}/L_{\text{EM}} = 1.1$, medium circles have $L_{\text{imp}}/L_{\text{EM}} = 1.2$, and large symbols (triangles and circles) have $L_{\text{imp}}/L_{\text{EM}} = 1.45$. In some cases data points are overlapping. Frames (a) through (e) show the same quantities as in Figs. 4 through 6.

momentum vector after the impact, i.e., $\vec{L}_{\text{imp}} = \vec{L}_{\text{col}} + \vec{L}_{\text{spin}}$. Consider a coordinate system (Fig. 10a) in which the positive z -axis is defined by the desired direction of \vec{L}_{imp} , the x - z plane is that which contains \vec{L}_{col} and \vec{L}_{spin} , and the polar angles associated with \vec{L}_{col} and \vec{L}_{spin} are θ_c and θ_s , respectively. I define the positive x -axis so that $0^\circ \leq \theta_s \leq 180^\circ$. Two simple relations apply:

$$\begin{aligned} L_{\text{imp}} &= |L_{\text{col}}| \cos \theta_c + |L_{\text{spin}}| \cos \theta_s, \\ 0 &= |L_{\text{col}}| \sin \theta_c + |L_{\text{spin}}| \sin \theta_s. \end{aligned} \quad (4)$$

The limiting “prograde” and “retrograde” cases discussed above would correspond to $\theta_c = 0^\circ$ and $\theta_s = 0^\circ$ or 180° . Fig. 10b compares results of all simulations with and without pre-impact spin

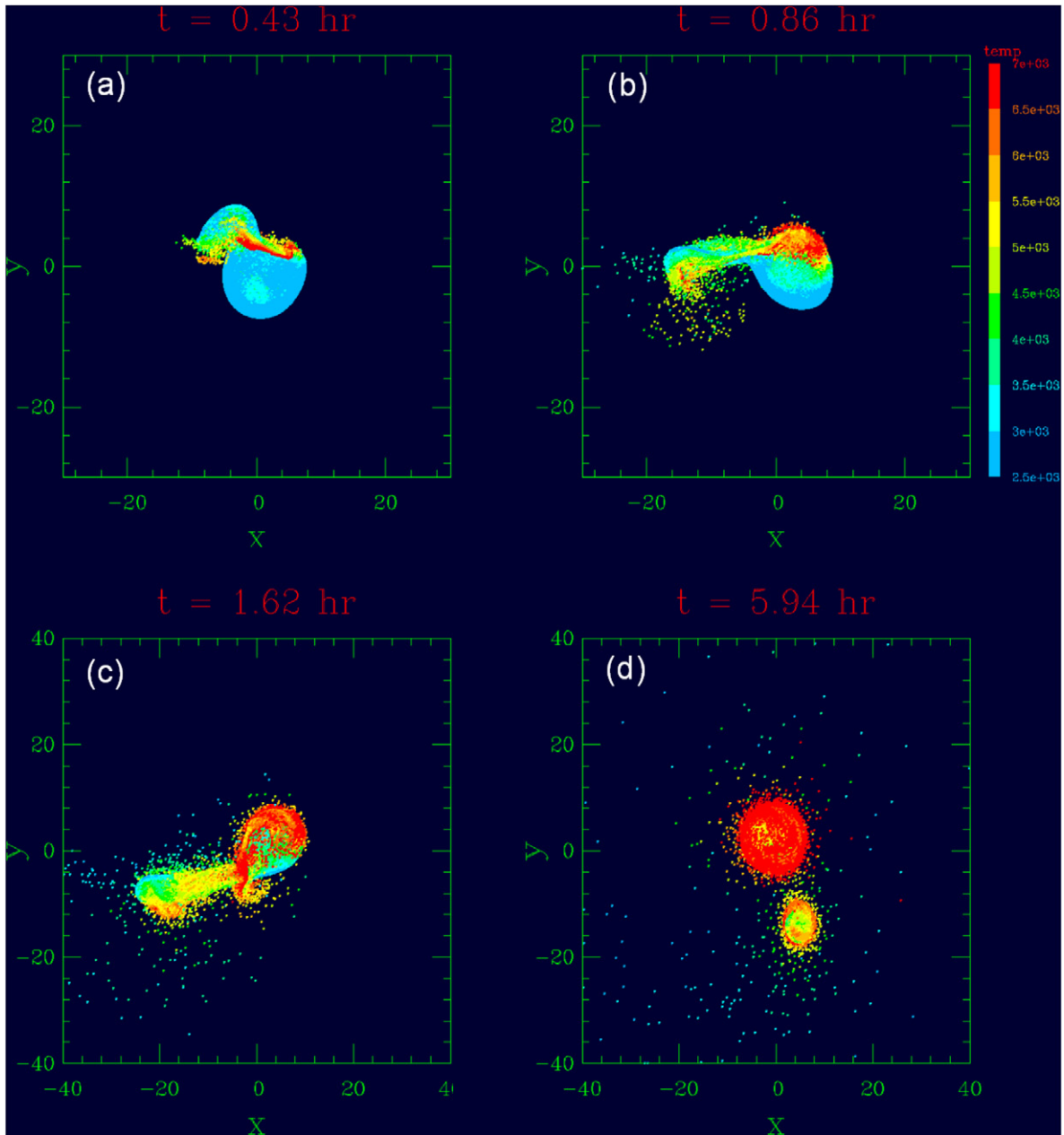


Fig. 8. An $N = 60,000$ particle simulation of an extreme case of a large impactor containing $0.2M_{\oplus}$ colliding with $v_{\text{imp}} = v_{\text{esc}}$ into a rapidly retrograde rotating target with a pre-impact spin period of 4 h (Run 87 in Table 1). Panels (a) through (f) show time steps viewed from above, with color scaling as temperature in degrees Kelvin and red particles having $T > 6500$ K. The final disk in (f) contains 2.1 lunar masses. (g) Mapping of particle final states (blue = in the planet, red = escaping, yellow = in the disk) onto the original figures of the target and impactor. (h) The difference between the peak temperature experienced by each particle and its initial temperature, mapped onto the figures of the target and impactor; red particles have $\Delta T > 10,000$ K.

in the protoearth that produced iron-depleted disks. The most favorable spin state is the retrograde, $\theta_s = 180^\circ$ case (black circles), with a wide range in rotation rates with this orientation yielding massive disks and $L_{\text{EM}} \leq L_F \leq 1.1L_{\text{EM}}$. Most of the prograde, $\theta_s = 0^\circ$ cases (gray circles) are unsuccessful, because they typically require smaller impactors and/or smaller impact parameters that yield less massive disks.

Intermediate values of θ_s that would also be favorable to forming the Moon can be estimated as a function of $|L_{\text{spin}}|$ in the pre-impact protoearth. Accounting for angular momentum loss in escaping material and later interactions with the Sun, a match with the Earth–Moon system requires $|L_{\text{imp}}| \sim 1.1$ to $1.25L_{\text{EM}}$. Given $|L_{\text{imp}}|$ and $|L_{\text{spin}}|$, allowable values for $|L_{\text{col}}|$ and θ_c can be solved for as a function of θ_s from Eq. (4). Fig. 10c shows

$|L_{\text{col}}|$ as a function of θ_s for three values of $|L_{\text{spin}}|$, assuming $|L_{\text{imp}}| = 1.2L_{\text{EM}}$. Simulations with or without pre-impact spin find that $|L_{\text{col}}| > 1.06L_{\text{EM}}$ is required to produce a sufficiently massive protolunar disk, with most of the successful cases here (Table 1) and in Canup (2004a) having $|L_{\text{col}}| > 1.2L_{\text{EM}}$. The gray horizontal line in Fig. 10c shows $|L_{\text{col}}| = 1.06L_{\text{EM}}$. For a slow pre-impact rotation in the protoearth (e.g., the $|L_{\text{spin}}| = 0.1L_{\text{EM}}$ short-dashed curve, corresponding to about a 40-h pre-impact terrestrial day prior to the lunar forming impact), any orientation for θ_s can be consistent with $|L_{\text{col}}| > 1.06L_{\text{EM}}$ and a potentially successful impact. However for a rapid pre-impact spin in the protoearth, θ_s must be substantial in order to allow for a sufficiently large value for $|L_{\text{col}}|$. For example, for $0.5 \leq |L_{\text{spin}}|/L_{\text{EM}} \leq 1.0$ (solid and long-dashed curves, corresponding to an approximately 4- to 8-h

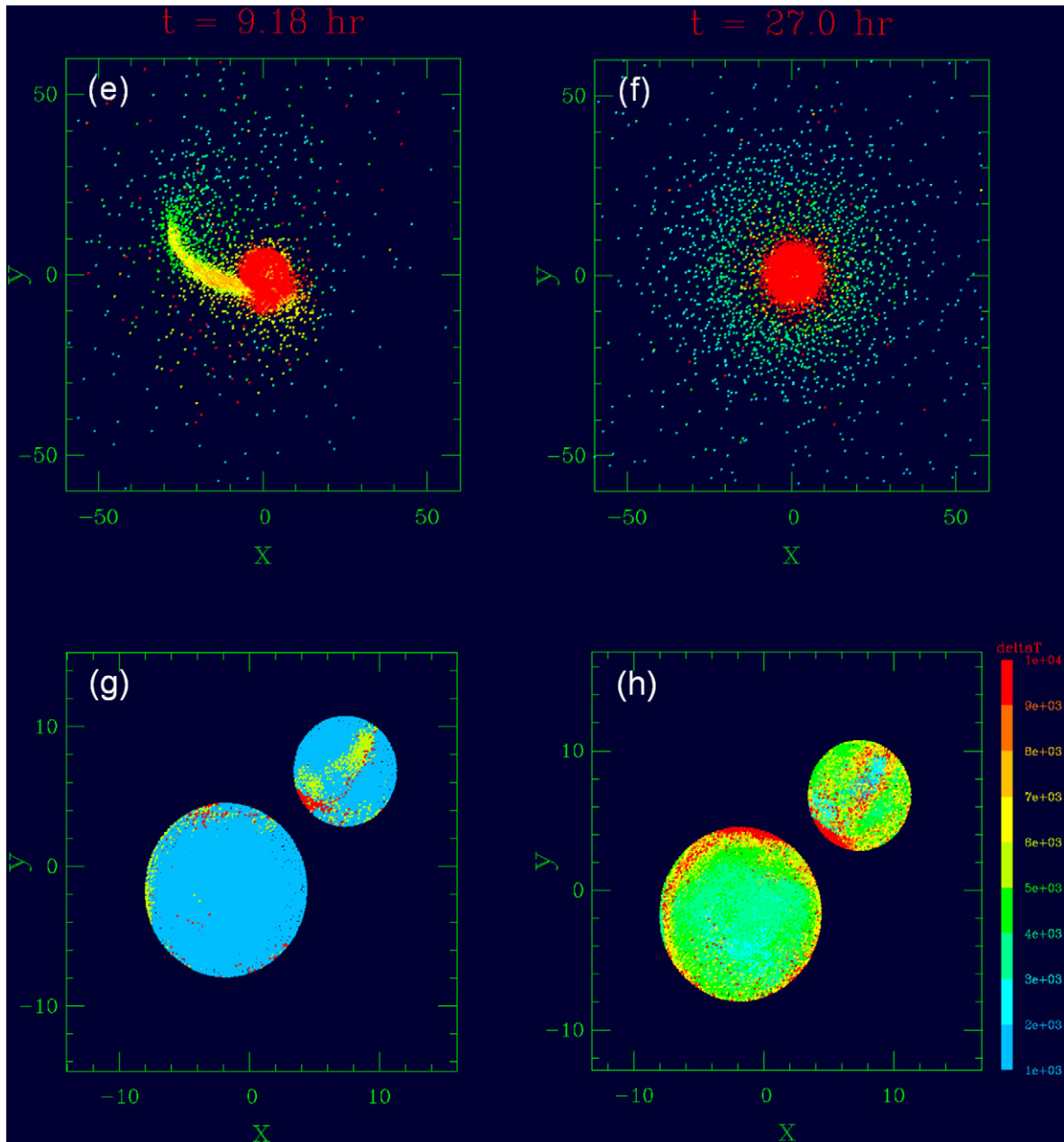


Fig. 8. (continued)

pre-impact terrestrial day), $\theta_s \gtrsim 60^\circ$ is required. In order for the orientation of \vec{L}_{imp} to be consistent with a post-impact obliquity for the Earth of $\theta_{\oplus} \leq 15^\circ$, a minimum pre-impact terrestrial obliquity $\sim 45^\circ$ is then implied. Still larger pre-impact obliquities would yield more favorable outcomes, as they allow for higher values for $|L_{\text{col}}|$ (Fig. 10c). Terrestrial accretion simulations (e.g., Agnor et al., 1999) predict an isotropic spin-axis distribution, and in this case obliquities near 90° are the most common.

5. Summary and discussion

Prior works consider non-rotating targets and impactors, assuming that the lunar-forming impact delivered the entire angular momentum of the Earth–Moon system. In this case, a range of successful candidate impacts has been identified that produces favorable conditions for forming the Moon (Canup and Asphaug, 2001; Canup, 2004a, 2004b). However, planet formation models suggest that the protoearth and impactor were likely rotating rapidly dur-

ing the late stages of their growth. This work has explored the effects of pre-impact rotation on lunar forming impacts, in particular to determine whether this can allow for less restrictive impact scenarios than those identified previously.

An exhaustive parameter space search of giant impacts involving pre-impact spins in the target and/or the impactor would be computationally prohibitive. As such I have focused on the limiting cases that I find have the greatest influence on impact outcome: a prograde or retrograde spin in the target that is aligned or anti-aligned with the collisional angular momentum vector. A pre-impact spin in the target that lacks a component parallel to the collisional angular momentum vector has much smaller effects on impact outcome, and resembles the non-spin cases. Rotation in the impactor is also less important, with impactor spin periods of 5 h or more altering the disk mass and angular momentum by less than 20% for a roughly Mars-sized impactor.

I define a “successful” impact as one in which the disk mass and angular momentum is sufficient to produce the Moon outside

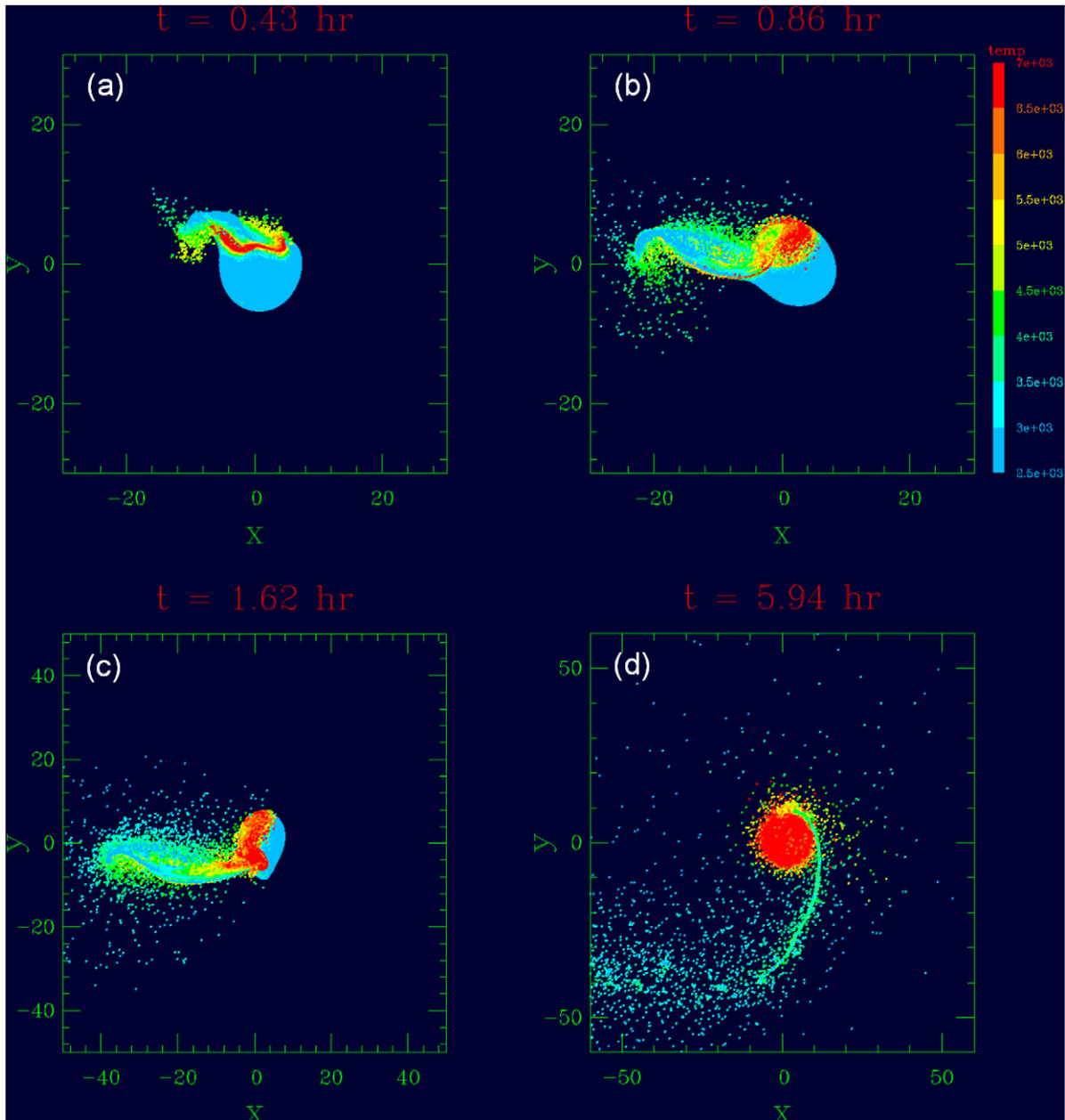


Fig. 9. An $N = 122,000$ particle simulation of an impactor with mass $0.13M_{\oplus}$ colliding with $v_{\text{imp}} = 1.05v_{\text{esc}}$ into a prograde rotating target with a pre-impact spin period of 56 h (Run 53p in Table 1). Panels (a) through (f) show time steps viewed from above, with color scaling as temperature in degrees Kelvin and red particles having $T > 6500$ K. The final disk in (f) comprises 1.28 lunar masses, with the largest clump represented by 450 SPH particles containing $0.16M_L$. (g) Mapping of particle final states (blue = in the planet, red = escaping, yellow = in the disk) onto the original figures of the target and impactor. (h) The difference between the peak temperature experienced by each particle during the impact and its initial temperature, mapped onto the figures of the target and impactor; red particles have $\Delta T > 10,000$ K.

the Earth's Roche limit, the disk iron mass fraction is 10% or less, and the final system angular momentum is $\leq 1.2L_{\text{EM}}$. Comparing successful cases with and without pre-impact spin, the key differences occur for cases involving a pre-impact retrograde rotation in the target, because these allow for larger impactors (up to $\gamma = 0.2$ vs $0.11 < \gamma < 0.15$ for the no-spin cases) and provide improved agreement between the final system angular momenta and that of the current Earth–Moon system.

Overall however, the properties of successful impacts with and without pre-impact rotation are remarkably similar. In this work I consider a relatively wide range in impact speeds, angles, and impactor masses, and the resulting collisions produce a correspondingly broad range of final planet–disk systems (e.g., Figs. 4–7). But a successful lunar-forming impact—with or without pre-impact spin—consistently requires a low-velocity collision with an im-

pector speed within 10% of the Earth's escape velocity, and an impact angle between about 40 and 50 degrees. Resulting protolunar disks contain up to about 2 lunar masses, are composed initially of melt together with ~ 10 to 30% vapor by mass, and are derived primarily (~ 60 to 90%) from material originating in the impactor's mantle. An impactor origin of the majority of protolunar material thus continues to be a universal prediction of all successful impact simulations, and must ultimately be reconciled with the identical O-isotope compositions of the Earth and Moon.

What limits can be placed on the rotational state of the protoearth prior to a Moon-forming giant impact? If the protoearth was rotating slowly, any pre-impact orientation of its spin axis can be consistent with a successful Moon-forming impact. However, if the protoearth was rotating rapidly before the giant impact, the re-

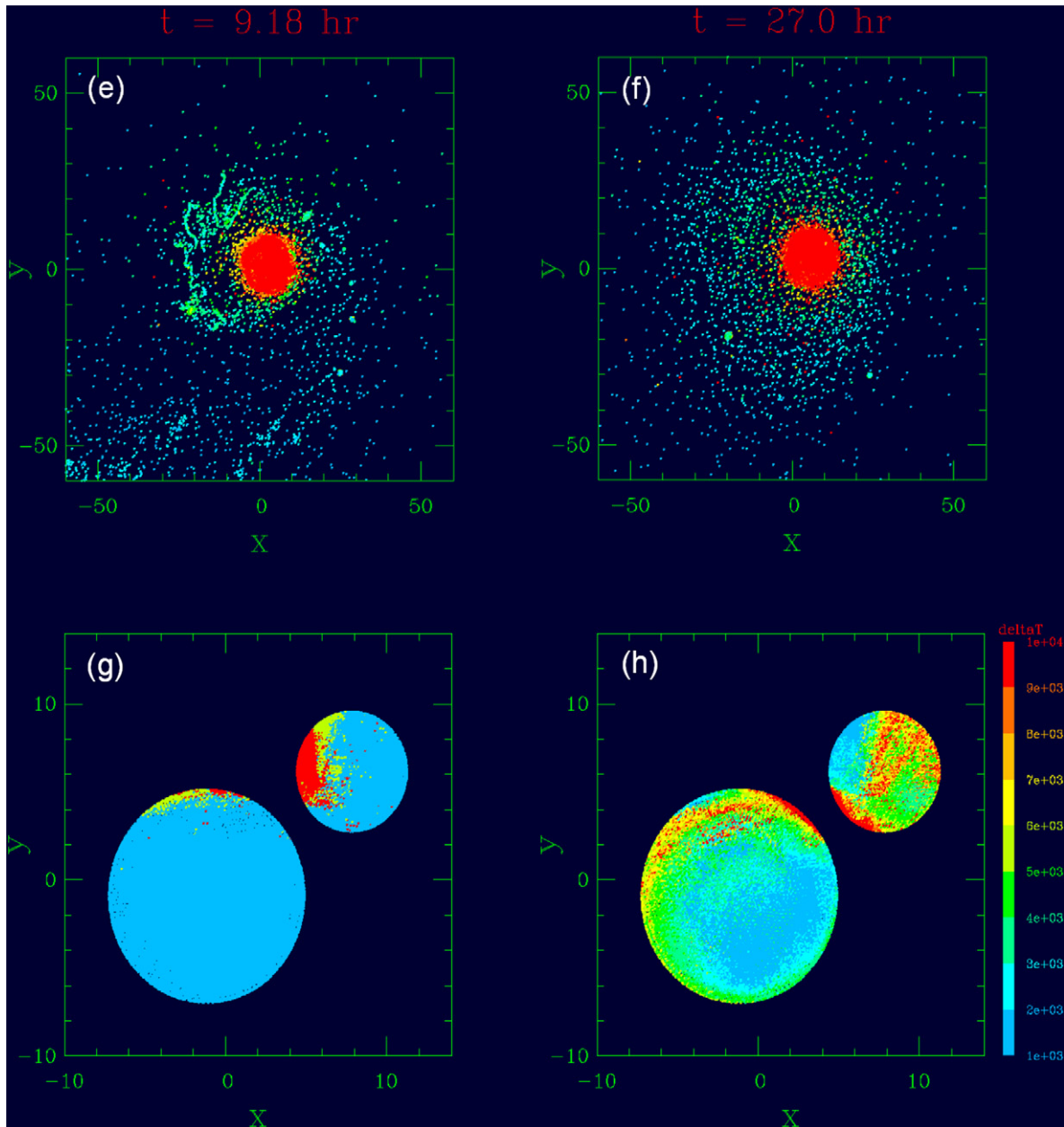


Fig. 9. (continued)

sults here imply that its obliquity must have been substantial. Creating a disk massive enough to produce the Moon requires that the angular momentum in the collision itself must be comparable to or somewhat larger than L_{EM} . For agreement with the current Earth–Moon, the impact needs to leave the system with a total angular momentum $< 1.1L_{EM}$, together with a relatively small, $\sim 7^\circ$ to 15° obliquity. The most problematic pre-impact state is a low obliquity, rapid prograde rotation in the protoearth. This state requires a smaller impactor and/or a less oblique impact to reproduce the Earth’s obliquity and the Earth–Moon system angular momentum, and these conditions produce disks that are not massive enough to yield the Moon. In contrast, a rapidly rotating protoearth with a large or even retrograde pre-giant impact obliquity provides favorable conditions for producing the Moon.

Acknowledgments

This paper is dedicated to Alastair Cameron, in recognition of his fundamental work on lunar origins and in appreciation for his

having inspired my interest in impact simulations. I thank Eiichiro Kokubo and an anonymous referee for their helpful and thorough reviews, Jay Melosh and Betty Pierazzo for providing me with M-ANEOS and the associated material parameter constants used here, and Amy Barr for comments on an earlier draft of the paper. This work benefited from Peter Tamblin’s assistance in development of some of the analysis software, and the computer support of Dirk Terrell, Peter Tamblin, and Norm Heinen at SwRI. Support from NASA’s Origins of Solar Systems program is gratefully acknowledged.

Appendix A. Effect of numerical resolution on impact outcome

A critical issue in the reliability of SPH results is numerical resolution. As an interpolative method, SPH requires many overlapping particles for accuracy, and SPH cannot resolve effects that occur on size scales comparable to or smaller than the characteristic particle smoothing length. For impacts like those here, whose outcomes are determined primarily by gravitational interactions,

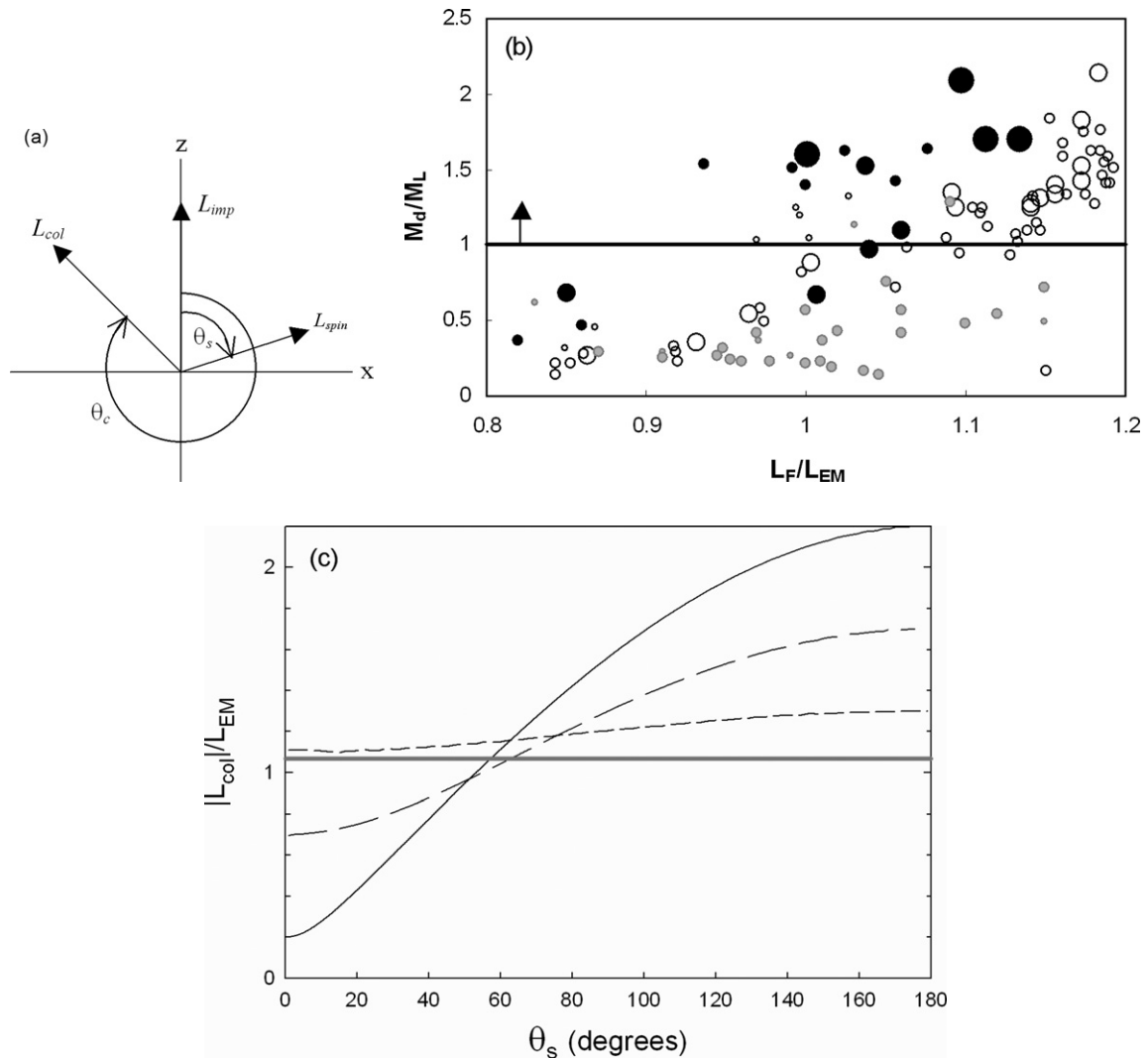


Fig. 10. (a) Angular momentum vectors associated with pre-impact spin (L_{spin}), the collision (L_{col}), and the total angular momentum after the impact (L_{imp}), where $\vec{L}_{imp} = \vec{L}_{col} + \vec{L}_{spin}$, and L_{imp} defines the direction of the positive z -axis (see text for details). (b) Results of impact simulations that all produced iron-depleted disks having $M_{Fe}/M_d \leq 0.1$. Black circles correspond to impacts into a retrograde rotating protoearth (with $\theta_c = 0^\circ$ and $\theta_s = 180^\circ$), open circles are cases without pre-impact spin (from Canup, 2004a), and gray circles are impacts into a prograde rotating protoearth (with $\theta_c = \theta_s = 0^\circ$). Symbol size scales with impactor size (small, $\gamma = 0.11$; medium, $\gamma = 0.13$; large, $\gamma = 0.15$; extra-large, $\gamma = 0.20$). Plotted is the disk mass in lunar masses vs the final angular momentum of the bound planet-disk system, L_F , in units of L_{EM} . (c) Allowable values for $|L_{col}|/L_{EM}$ are shown as a function of θ_s for $|L_{spin}|/L_{EM} = 0.1$ (short-dashed curve), 0.5 (long-dashed curve) and 1.0 (solid curve). The horizontal gray line is $|L_{col}|/L_{EM} = 1.06$, the minimum value necessary for a successful lunar-forming collision based on simulations here and in Canup (2004a).

convergence of the results requires adequate resolution of the spatial distribution of impactor material after the initial impact, as well as the distorted figure of the post-impact protoearth. Vaporization must also be correctly modeled to account for pressure gradients and their effects on orbital emplacement, although in simulations to date vaporization processes appear less important effect than gravitational torques in determining overall impact outcomes (e.g., Canup, 2004a, 2004b).

Fig. A1 shows results of simulations at four resolutions ($N = 3 \times 10^4$, 6×10^4 , 1.2×10^5 , and 2.3×10^5) of the collision “Earth 119” (shown in Fig. 2 of Canup, 2004a), with $\gamma = 0.13$, $M_T = 1.019M_\oplus$, $b' = 0.73$, and $v_{imp} = v_{esc}$. Each simulation was continued until the outer clump of impactor material re-collides with the protoearth in a grazing impact and then shears out into the disk (as occurs between Figs. 2i through 2k in Canup, 2004a). The disk mass, disk angular momentum, mass of disk vapor, and mass of disk iron computed at this point show no systematic variation with increasing resolution for $N \geq 60,000$. Similar insensitivities were found in Canup (2004a, Fig. 8) for $20,000 \leq N \leq 120,000$.

Appendix B. Analytical approximation for mass placed in orbit as a function of b' and γ

The fraction of the colliding mass placed into orbit about the primary for low-velocity, gravity-regime impacts increases with impact parameter, b' , and is derived predominantly from impactor material that grazes past the target during the initial impact (e.g., Figs. 3c–3d in Canup, 2004a; Figs. 8g and 9g here). Immediately post-impact, this portion of the impactor forms an elongated bar of debris, which through Keplerian rotation winds up into a trailing arm relative to the rotational sense of the impact. The self-gravity of this configuration leads to a net transfer of angular momentum from inner, leading material to the trailing, outermost material, with the latter overwhelmingly supplying the orbiting disk (e.g., Figs. 2c–2e). In addition, the distortion on the target’s surface due to the shock wave from the impact typically rotates ahead of the ejected debris, also providing a positive torque. While the details of these processes vary considerably from case to case, the observed consistency in the overall trends relating the final disk mass to b' and γ motivate the development of an analytical approximation.

The gravitational torque associated with a trailing spiral wave is proportional to the square of its surface density (e.g., Lynden-Bell

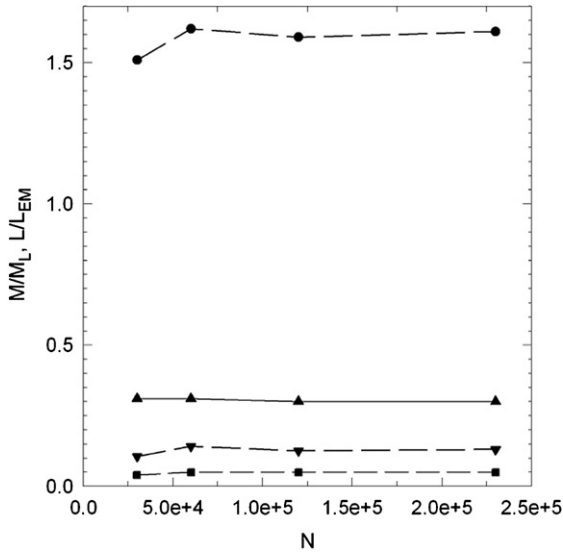


Fig. A1. Results of a lunar-forming impact simulation shown as a function of the total number of SPH particles. Circles, upside down triangles, and squares indicate the disk mass, the mass of vapor in the disk, and the mass of orbiting iron, respectively, all in units of a lunar mass. The triangles connected by the solid line indicate the disk angular momentum in units of the angular momentum of the current Earth–Moon system, L_{EM} .

and Kalnajs, 1972). To the extent that a similar torque is responsible for the emplacement of mass into orbit, one would expect the orbiting mass to vary as the square of the mass within the post-impact arm of debris, which in turn would be approximately proportional to the square of the mass of the impactor that avoids direct collision with the target. Here I calculate this mass as a function of b' and γ , and use this relation to derive an approximate expression for the orbiting mass produced by a low-velocity oblique impact.

Consider an impact occurring along the x -axis (Fig. B1a). The scaled impact parameter b' defines the distance Y' between the centers of the impactor and target, with $Y' \equiv b'(R_{tar} + R_i)$, where R_{tar} and R_i are the target and impactor radii. I first consider circular “slices” through the impactor of thickness dx and radius r_i (Fig. B1a), calculating for each slice the area that overlaps with the target as a function of b' and R_{tar} . Summing over these areas as the entirety of the impactor moves past the target gives the volume of the impactor that collides with the target, which is then used to determine the mass of the impactor that avoids direct collision. For simplicity, the calculation assumes $\vec{v} = v_x$ (and that the impactor maintains this velocity direction as it shears through the target), and that the impactor and target are spherical (i.e., distortion due to either tidal interaction or the collision itself is ignored).

Fig. B1b shows a circular slice of the impactor of radius r_i in the z - y frame. It is helpful to perform a coordinate transform into the \tilde{z} - y frame (Fig. B1b), where the \tilde{z} -axis is shifted below the z -axis by a distance $y_1 = r_i \cos \theta_0$, where $\theta_0 = \cos^{-1}[(Y'^2 + r_i^2 - R_{tar}^2)/2Y'r_i]$, and $y_1 + y_2 = Y'$. The area of overlap—the “lens”

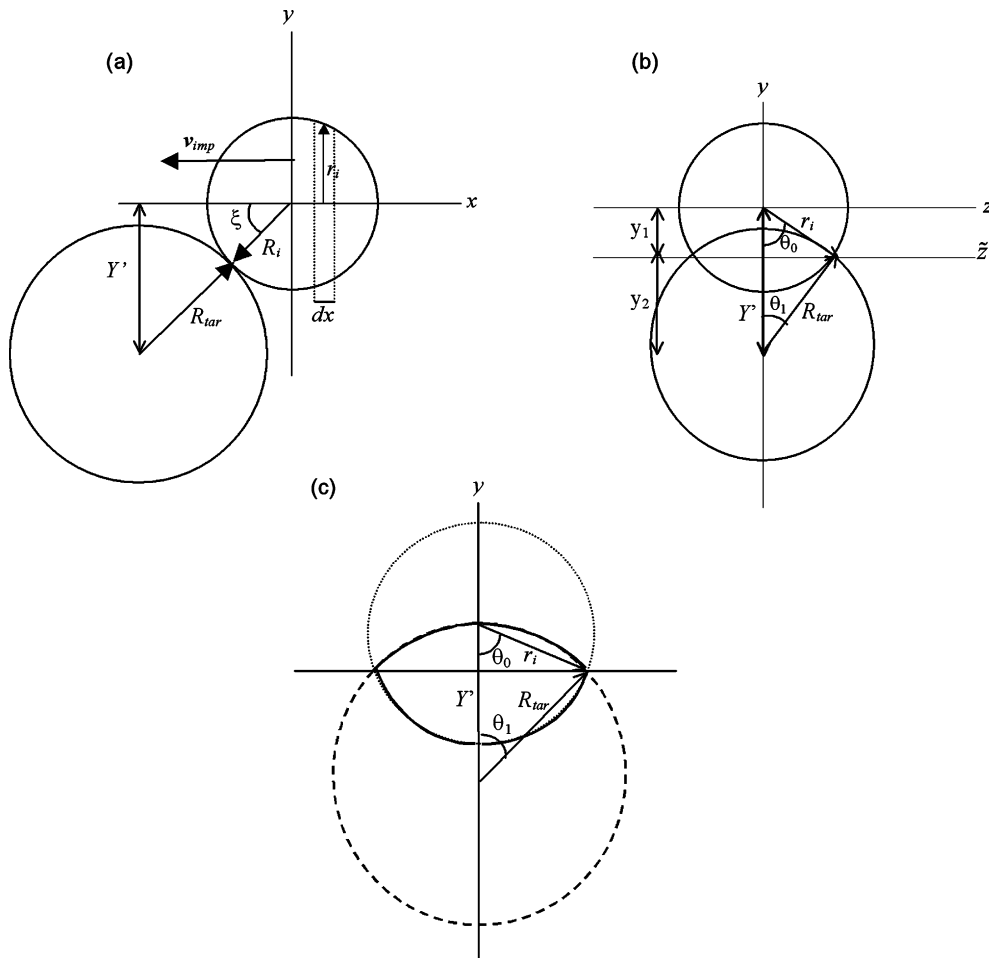


Fig. B1. Schematics for the calculation of the fraction of the impactor's mass that collides with vs misses the target during a collision. See text for details.

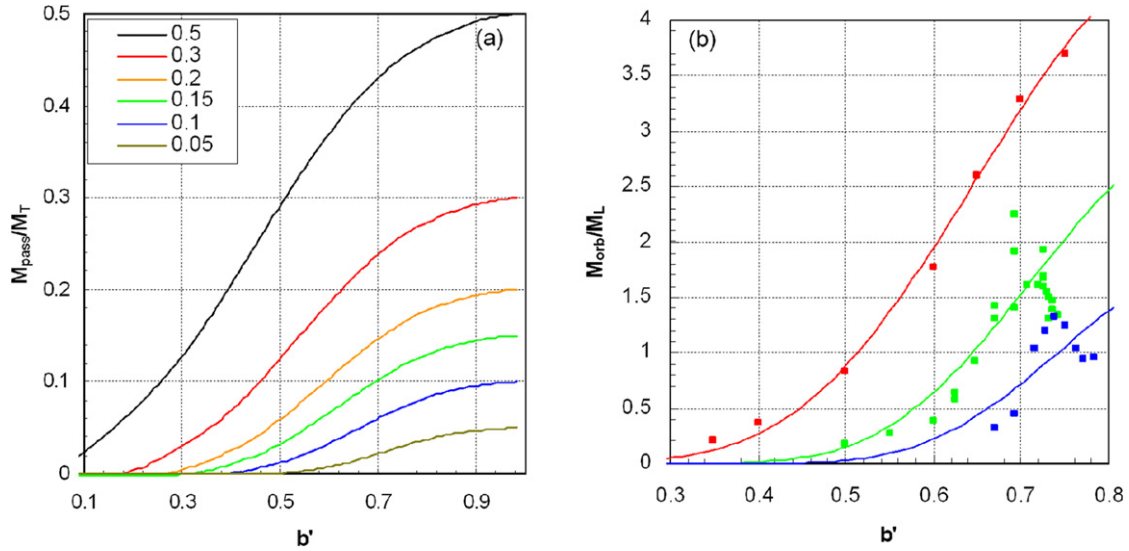


Fig. B2. (a) Mass of impactor that avoids direct collision with the target, M_{pass} , scaled to the total colliding mass M_T , as a function of γ (colored lines, γ -values shown in legend) and b' . (b) Curves estimating the orbiting mass in lunar masses produced by a collision with Eq. (3) for three γ values ($\gamma = 0.1, 0.15$ and 0.3) with $M_T \approx M_{\oplus}$. Results from SPH simulations with $v_{\text{imp}} \sim v_{\text{esc}}$ and no pre-impact spin are shown as squares (from Canup, 2004a and this work).

between the thick solid curves in Fig. B1c—can be computed geometrically. The upper half of the lens has an area

$$A_u(r_i) = 2 \left[\pi R_{\text{tar}}^2 \left(\frac{\theta_1}{2\pi} \right) - \frac{1}{2} (R_{\text{tar}} \cos \theta_1) (R_{\text{tar}} \sin \theta_1) \right], \quad (\text{B.1})$$

and similarly the lower half has an area

$$A_l(r_i) = 2 \left[\pi r_i^2 \left(\frac{\theta_0}{2\pi} \right) - \frac{1}{2} (r_i \cos \theta_0) (r_i \sin \theta_0) \right], \quad (\text{B.2})$$

so that the total overlapping area is

$$A(r_i) = A_u(r_i) + A_l(r_i) = R_{\text{tar}}^2 \theta_1 + r_i^2 \theta_2 - Y' r_i \sin \theta_0, \quad (\text{B.3})$$

where the relation $r_i^2 = R_{\text{tar}}^2 + Y'^2 - 2R_{\text{tar}}Y' \cos \theta_1$ has been used. Equation (B.3) is then integrated numerically with $r_i = R_i \sin \phi$, as ϕ is varied from 0 to π , to give the total impactor volume that collides with the target, $V_T(b', R_{\text{tar}}, R_i)$.

To estimate the colliding mass for a differentiated impactor, the above calculation is repeated for $R_i = R_{\text{core}}$, where $R_{\text{core}} \approx 0.5R_i$ (for a 30% iron, 70% dunite object) is the impactor core radius, which gives the volume of the impactor's core that directly collides with the target, V_{Fe} . The colliding volume of impactor mantle is then $V_{\text{Si}} = V_T - V_{\text{Fe}}$, so that the mass of the impactor that collides with the target is $M_{\text{hit}} = \rho_{\text{Fe}}V_{\text{Fe}} + \rho_{\text{Si}}V_{\text{Si}}$, and the impactor mass that misses the target is $M_{\text{pass}} = M_i - M_{\text{hit}}$. Fig. B2a shows predicted values for (M_{pass}/M_T) as a function of b' for several values of $\gamma \equiv M_i/M_T$. As the scaled impact parameter b' approaches zero (a head-on impact), the entire impactor collides with the target and $(M_{\text{pass}}/M_T) \rightarrow 0$, while as $b' \rightarrow 1$, the impactor completely grazes the target and $(M_{\text{pass}}/M_T) \rightarrow \gamma$.

Fig. B2b shows results of impact simulations with low velocities ($v_{\text{imp}} < 1.1v_{\text{esc}}$) without pre-impact spin. The orbiting mass can be approximated as

$$\frac{M_{\text{orb}}}{M_T} \sim C_\gamma \left(\frac{M_{\text{pass}}}{M_T} \right)^2, \quad (\text{B.4})$$

where (M_{pass}/M_T) is given in Fig. B2a, and $C_\gamma \sim 2.8(0.1/\gamma)^{1.25}$, where C_γ has been determined empirically from the SPH data and reflects that a larger fraction of (M_{pass}/M_T) is placed in orbit as γ is decreased. For a fixed value of (M_{pass}/M_T) , a smaller γ collision is more grazing (e.g., Fig. B2a) and the outermost portions of the impactor that miss the target are at a greater distance

from the surface of the target, so that they are decelerated less during the initial impact than in a larger γ collision having the same (M_{pass}/M_T) . Equation (B.4) is valid to better than a factor of 2 for collisions involving terrestrial composition objects with $0.4 \leq b' \leq 0.7$ and $1 \leq (v_{\text{imp}}/v_{\text{esc}}) \leq 1.4$, and for $0.4 \leq b' \leq 0.8$ for low impact velocities ($1 \leq (v_{\text{imp}}/v_{\text{esc}}) \leq 1.1$).

References

- Agnor, C.B., Asphaug, E., 2004. Accretion efficiency during planetary collisions. *Astrophys. J.* 613, L157–L160.
- Agnor, C.B., Canup, R.M., Levison, H.F., 1999. On the character and consequences of large impacts in the late stage of terrestrial planet formation. *Icarus* 142, 219–237.
- Benz, W., Cameron, A.G.W., Melosh, H.J., 1989. The origin of the Moon and the single impact hypothesis III. *Icarus* 81, 113–131.
- Cameron, A.G.W., 2000. Higher-resolution simulations of the giant impact. In: Canup, R.M., Righter, K. (Eds.), *Origin of the Earth and Moon*. Univ. of Arizona Press, Tucson, pp. 133–144.
- Cameron, A.G.W., Ward, W.R., 1976. The Origin of the Moon. *Lunar Planet. Sci.* VII, 120–122.
- Canup, R.M., 2004a. Simulations of a late lunar forming impact. *Icarus* 168, 433–456.
- Canup, R.M., 2004b. Formation of the Moon. *Annu. Rev. Astron. Astrophys.* 42, 441–475.
- Canup, R.M., 2005. A giant impact origin of Pluto–Charon. *Science* 307, 546–550.
- Canup, R.M., Asphaug, E., 2001. Origin of the Moon in a giant impact near the end of the Earth's formation. *Nature* 412, 708–712.
- Canup, R.M., Ward, W.R., Cameron, A.G.W., 2001. A scaling relationship for satellite-forming impacts. *Icarus* 150, 288–296.
- Clayton, R.N., 1993. Oxygen isotopes in meteorites. *Annu. Rev. Earth Planet. Sci.* 21, 115–149.
- Goldreich, P., 1966. History of the lunar orbit. *Rev. Geophys.* 4, 411–439.
- Ida, S., Canup, R.M., Stewart, G.R., 1997. Lunar accretion from an impact generated disk. *Nature* 389, 353–357.
- Jones, J.H., Delano, J.W., 1989. A three-component model for the bulk composition of the Moon. *Geochim. Cosmochim. Acta* 53, 513–527.
- Jones, J.H., Palme, H., 2000. Geochemical constraints on the origin of the Earth and Moon. In: Canup, R.M., Righter, K. (Eds.), *Origin of the Earth and Moon*. Univ. of Arizona Press, Tucson, pp. 197–216.
- Kaula, W.M., Yoder, C.F., 1976. Lunar orbit evolution and tidal heating of the Moon. *Lunar Planet. Sci.* XVII, 440–442.
- Kokubo, E., Makino, J., Ida, S., 2000. Evolution of a circumterrestrial disk and formation of a single moon. *Icarus* 148, 419–436.
- Lucey, P.G., Taylor, G.J., Malaret, E., 1995. Abundance and distribution of iron on the Moon. *Science* 268, 1150–1153.
- Lucy, L.B., 1977. A numerical approach to the testing of the fission hypothesis. *Astron. J.* 82, 1013–1024.
- Lynden-Bell, D., Kalnajs, A.J., 1972. On the generating mechanism of spiral structure. *Mon. Not. R. Astron. Soc.* 157, 1–30.

- Melosh, H.J., 2000. A new and improved equation of state for impact computations. *Lunar Planet. Sci.* XXXI, 1903.
- Melosh, H.J., 2008. A hydrocode equation of state for SiO₂. *Meteor. Planet. Sci.*, submitted for publication.
- Ohtsuki, K., Ida, S., 1998. Planetary rotation by accretion of planetesimals with non-uniform spatial distribution formed by the planet's gravitational perturbation. *Icarus* 131, 393–420.
- Pahlevan, K., Stevenson, D., 2007. Equilibration in the aftermath of the lunar-forming giant impact. *Earth Planet. Sci. Lett.* 262, 438–449.
- Schlichting, H.E., Sari, R., 2007. The effect of semicollisional accretion on planetary spins. *Astrophys. J.* 658, 593–597.
- Tillotson, J.H., 1962. Metallic equations of state for hypervelocity impact. Rep. GA-3216, July 18, Gen At., San Diego, CA.
- Thompson, C., Stevenson, D.J., 1988. Gravitational instability in two-phase disks and the origin of the Moon. *Astrophys. J.* 333, 452–481.
- Thompson, S.L., Lauson, H.S., 1972. Improvements in the Chart-D radiation hydrodynamic code III: Revised analytical equation of state. Technical Rep. SC-RR-710714, Sandia Nat. Labs.
- Touma, J., Wisdom, J., 1994. Evolution of the Earth–Moon system. *Astron. J.* 108, 1943–1961.
- Touma, J., Wisdom, J., 1998. Resonances in the early evolution of the Earth–Moon system. *Astron. J.* 115, 1653–1663.
- Vickery, A.M., Melosh, H.J., 1987. Orbital evolution of the vapor jet from a giant impact. *Lunar Planet. Sci.* XVIII, 1042–1043.
- Wada, K., Kokubo, E., Makino, J., 2006. High-resolution simulations of a Moon-forming impact and postimpact evolution. *Astrophys. J.* 638, 1180–1186.
- Wiechert, U., Halliday, A.N., Lee, D.-C., Synder, G.A., Taylor, L.A., Rumble, D., 2001. Oxygen isotopes and the Moon-forming giant impact. *Science* 294, 345–348.